Journal of Computational Physics 228 (2009) 6268–6290

Contents lists available at ScienceDirect

Journal of Computational Physics

journal homepage: www.elsevier.com/locate/jcp

On numerical realizability of thermal convection

Zbigniew P. Piotrowski [a,b], Piotr K. Smolarkiewicz [c,*], Szymon P. Malinowski [a], Andrzej A. Wyszogrodzki [c]

[a] Institute of Geophysics, University of Warsaw, Warsaw, Poland
[b] Institute of Meteorology and Water Management, Warsaw, Poland
[c] National Center for Atmospheric Research, Boulder, CO 80307, USA

ARTICLE INFO

Article history:
Received 24 January 2009
Received in revised form 23 April 2009
Accepted 12 May 2009
Available online 20 May 2009

PACS:
92.60.Aa
92.60.Fm
92.60.Hk
47.27.Ep

Keywords:
Convection organization
Turbulence parameterization
Large-eddy-simulation
Non-oscillatory differencing

ABSTRACT

Astounded at the regularity of convective structures observed in simulations of mesoscale flow past realistic topography, we investigate the computational aspects of a classical problem of flow over a heated plane. We find that the numerical solutions are sensitive to viscosity, either incorporated a priori or effectively realized in computational models. In particular, anisotropic viscosity can lead to regular convective structures that mimic naturally realizable Rayleigh–Bénard cells, which are unphysical for the specified external parameter range. Details of the viscosity appear to play a secondary role; that is, similar structures can occur for prescribed constant viscosities, explicit subgrid-scale turbulence models, ad-hoc numerical filters, or implicit dissipation of numerical schemes. This implies the need for a careful selection of numerical tools suitable for convection-resolving simulations of atmospheric circulations. The implicit large-eddy-simulation (ILES) approach using non-oscillatory schemes is especially attractive, as for under-resolved calculations it reproduces well the coarsened results of finely-resolved boundary layer convection.

1. Introduction

Numerical simulation is one of a few tools available for quantitative prediction of natural thermal convection and the associated phenomena occurring on scales from laboratory [1], to planetary [2], to stellar [3]. However, for low and moderate Rayleigh numbers[1] even a qualitative realization of thermal convection depends critically on problem parameters, thus allowing discontinuous transitions (bifurcations) in the solution phase space [4]. Consequently, in under-resolved calculations some otherwise negligible inadequacies of numerical approximations may lead to substantial departures from observed realizations.

As resolution and grid spacing of numerical models improve, atmospheric numerical weather prediction (NWP) enters the phase where traditional convection parameterization [5] becomes obsolete and is replaced with a cloud-resolving approach. Explicit simulation of convective cloud fields is no longer in the realm of research models [6–8], but with horizontal grid spacing $\mathcal{O}(10^3)$ m it enters the domain of the operationally practical NWP codes [9,10]. Although this eliminates some uncertainties associated with phenomenological parameterizations and gives a more accurate picture of the physics of convective systems [11,12], the $\mathcal{O}(10^3)$ m spacing is still too coarse, compared to $\mathcal{O}(10)$ m to $\mathcal{O}(10^2)$ m values appropriate for

* Corresponding author. Tel.: +1 303 497 8972; fax: +1 303 497 8181.
E-mail address: smolar@ucar.edu (P.K. Smolarkiewicz).

[1] We refer to barely larger than critical Rayleigh numbers as "low"; whereas "moderate" denotes values sufficiently large to admit a range of unstable modes, yet orders of magnitude smaller than representative of planetary and solar atmospheres.

0021-9991/$ - see front matter © 2009 Elsevier Inc. All rights reserved.
doi:10.1016/j.jcp.2009.05.023

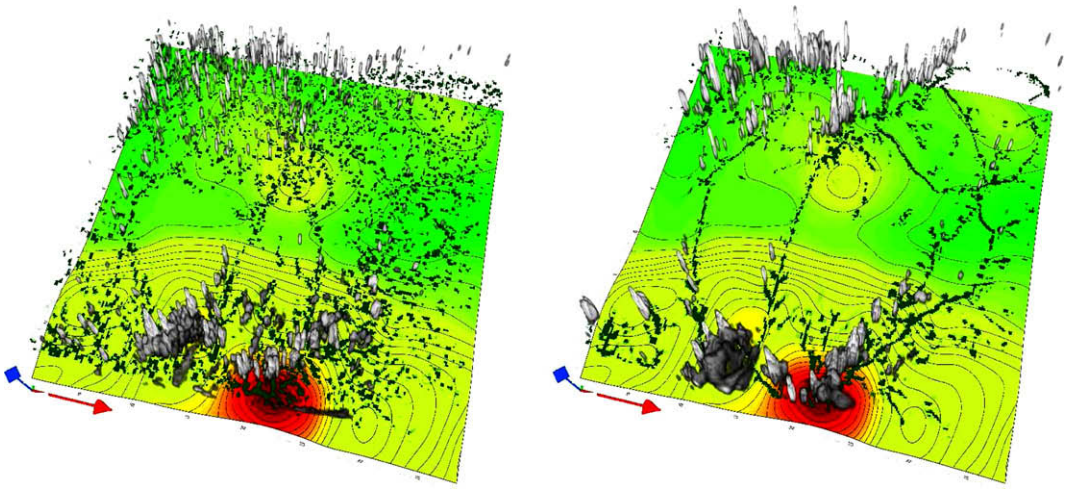

Fig. 1. Convection over heated terrain after 6 h of simulated daytime. Grey iso-surfaces represent clouds, dark green patterns mark updrafts at the top of PBL, and light green isolines depict the terrain. The two panels correspond to two simulations with different effective viscosity of numerical advection, but are identical otherwise.

large-eddy-simulation of shallow and deep convection [13,14]. As a consequence, the simulated cloud fields are sensitive to subgrid-scale models and numerical approximations employed. This in turn influences simulated weather and climate, due to their dependence on cloud field structure via precipitation and radiation.

The organization of atmospheric convection is observed over a range of scales from hundreds of meters (convective cells), hundreds of kilometers (mesoscale systems, fronts), up to planetary scale (Madden–Julian oscillation). Convection may be organized, e.g. by planetary waves [15], interaction between air masses with different properties [16], orography [17,18], or simply in response to surface thermal forcing [19]. The latter typically results in either roll or cell type organization, which most often occurs in maritime conditions [16] but can be also observed over land [20,21]. Because initiation of such an organization depends on the development of the boundary layer beneath, studies of the planetary boundary layer (PBL) with a wide range of convective phenomena, occurring on scales from $\mathcal{O}(10^2)$ m [22] to $\mathcal{O}(10^4)$ m [23], are important for understanding and forecasting atmospheric convection.

In practical terms this paper alludes to weather prediction with explicit treatment of moist convective processes. It stems from an earlier study of a natural mesoscale flow [24], wherein the authors highlighted a series of multi-scale simulations of fair weather over southern Poland. The routine hydrostatic mesoscale predictions at 17 km resolution, using the Unified Model for Poland Area (UMPL) [25], continuously supplied the initial, boundary and ambient conditions for high-resolution simulations using the nonhydrostatic anelastic model EULAG [26]. The EULAG domain 240×200 km^2 embedded in the UMPL Central European domain (2000×2400 km^2) was covered with 4, 2 and 1 km horizontal grid intervals, while keeping twice the vertical resolution of UMPL. The comparison of simulated cloud fields with satellite images suggested that the overall location and timing of moist convection was captured in all simulations. Furthermore, as the resolution of the EULAG domain improved, the representation of convective clouds appeared increasingly more realistic. In particular, at horizontal grid intervals 2 km and smaller, irregular Rayleigh–Bénard like cells emerged in simulated boundary layers, Fig. 1.[2] In spite of a feasible appearance the cellular updraft patterns were judged dubious, especially those evident in the right panel of Fig. 1. A thorough investigation with many reductions toward the essential simplicity (Fig. 2) disclosed a dominant influence of the truncation terms in advective transport operators. The emergence of cellular patterns turned out to be related to filtering the transported variables by the non-oscillatory MPDATA advection [28,29] used in the spirit of the composite-schemes approach of Liska and Wendroff [30,31].[3]

It is well known that the numerical realizations of simulated physical phenomena may depend critically on the algorithms employed. The literature documenting various forms of numerical artifacts disguised as physical effects is rich and interdisciplinary; see [32–34] for examples. Here, we report on a systematic investigation of numerical effects that influence the structure of simulated convection in the PBL. Specifically, we focus on effective viscosity and diffusivity representative of contemporary numerical models. We compare and classify flow responses to various realizations of viscous effects, and examine them against linear estimates. Looking forward toward petascale computing, we draw conclusions regarding the potential utility of selected modern numerical approaches for cloud-resolving NWP.

In the next section the theoretical estimates are discussed using the arguments of small-perturbation linear theories, to aid in the interpretation of numerical results. Section 3 describes the computational model employed. The parameters of the

[2] Figs. 1 and 2 were generated using VAPOR, a new tool for the scientific investigation of massive computational data sets [27].

[3] The default second-order accuracy of MPDATA was reduced to the first-order using the generic upwind scheme every fourth time step.

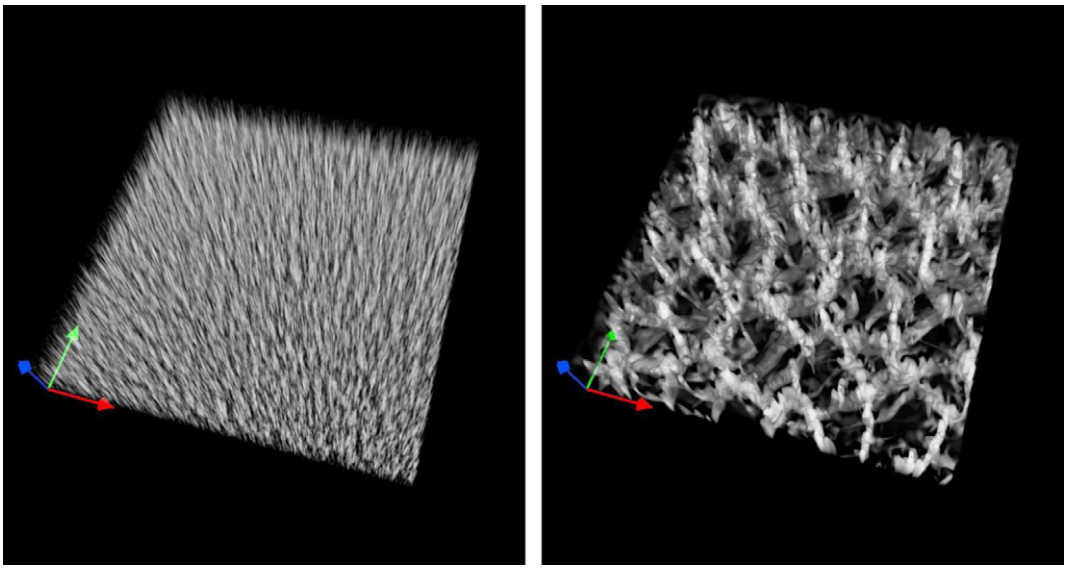

Fig. 2. Structure of thermal convection over heated plane. Vertical velocities after 6 h of simulated time are shown within the PBL depth; bright volumes denote updrafts. The only difference between the two solutions is the value of viscosity in the horizontal.

numerical experiment, results of the reference simulation, and the structural convergence analysis are presented in Section 4. Effects of numerical truncation and interpretation of associated artifacts, in terms of linear solutions, are presented in Section 5. Section 6 concludes the paper.

2. Theoretical considerations

2.1. Historical background

A great deal of the theoretical knowledge on thermal convection comes from linear theories. The fundamental work of Rayleigh [35] set the scope with an attempt to examine Bénard's laboratory results [36] in terms of the interplay between the action of buoyant and viscous processes within a fluid layer of finite vertical extent and unstable stratification.[4] Rayleigh deduced a marginal stability condition stating that unless $-N^2H^4/\kappa\nu$ is larger than a certain critical value ($\approx 10^3$ depending on the boundary conditions [37,38]) the fluid is in stable equilibrium; i.e., no development of convective elements is possible. Here, N denotes the buoyancy frequency (imaginary), H is the vertical extent of the fluid, and ν and κ are kinematic viscosity and thermal diffusivity. For unstable conditions, however, seeking prevailing symmetric modes leads to cellular structures (Section 16 in [37]) — sensitive, nonetheless, to physical conditions (Section 2.5 in [19]). The linear theory of Rayleigh has been extended and organized over decades; for complementary expositions and insights see classical monographs [37–39].

Although the Rayleigh theory does not formally address atmospheric mesoscale convection, it has inspired numerous related works relying on arguments of effective eddy-viscosity in lieu of molecular material constants. One of the early attempts was made by Jeffreys [40] who proposed an effective Rayleigh number $Ra = -N^2H^4/\kappa_e\nu_e = \mathcal{O}(10^3)$, where subscript "$e$" refers to eddy values. The advent of satellite meteorology reinvigorated interests in the structure of atmospheric convection. Priestley [41], inspired by an observational study [42], proposed that anisotropic turbulent viscosity may be responsible for cellular structures of mesoscale convection, the aspect ratio of which departs from the laboratory values by one order of magnitude. Furthermore, he provided heuristic arguments that the dimensions of cellular structures should scale as the square root of the entries of a diagonal viscosity tensor. The analytic solution in the spirit of the Rayleigh linear theory, but admitting anisotropy of viscous terms (e.g. $\nu_j\partial^2\vec{u}/\partial x_j^2$) was first shown by Ray [43]. He illustrated the resulting marginal stability condition numerically, obtaining the observed convective-cell aspect ratio (about 30 times wider than deep) for various combinations of ν_j, typically requiring horizontal values ν_1 and ν_2 two to three orders of magnitude larger than ν_3. Later Sheu et al. [44] corroborated Priestley's scaling arguments with linear theory and nonlinear 2D calculations. The role of anisotropic eddy-viscosity in the evolution of convective structures has been studied over decades in the context of atmospheric and oceanic flows [43–47]. In general, the convective response has been found to be sensitive to the magnitude, the inhomogeneity and the anisotropy of viscous forcings. Nonetheless, according to the review in [23] the influence of eddy-viscosity on cellular convection in the atmosphere is still an open question.

[4] Serendipitously, the Bénard experiment captured thermocapillary convection, with instability due to the temperature dependence of the surface tension; cf. Chapter 1 in [19].

In this paper we address a similar problem, yet approached from a different angle. We only touch upon the role of theoretical turbulence models in the evolution of convective fields, as our primary concern is the convective response to filtering embedded in numerical models. This is an important issue, since computational models are leading tools for the prediction of, and policy making for, climatic changes. In the next section we turn to linear theory for insights on effects due to the anisotropy of viscous forcings. Because of our interest in the numerical realizability of thermal convection, we do not rigorously follow the Navier–Stokes formulation of the stress tensor [45] but instead exploit a simpler ad hoc model with anisotropic Laplacian contributions in the horizontal and the vertical, in the spirit of earlier works [41,43,44]. However, in contrast to these earlier works, the computational scope of the present work stimulates a different perspective, including the connection to physically aberrant asymptotics and growth rates of unstable modes — facilitating the interpretation of 3D simulation results.

2.2. Linear estimates

Linear solutions for uniform viscosity have been thoroughly discussed in the classical literature [37–39]. Here we highlight only the key steps, while referring the interested reader to earlier works. As in the classical theory, we assume the incompressible Boussinesq system linearized around a static reference state, but allow for different dissipative/diffusive forcings in the horizontal and the vertical

$$\begin{aligned}
&\frac{\partial \mathbf{u}}{\partial t} = -\nabla\phi + g\alpha\theta\nabla z + \nu_h \Delta_h \mathbf{u} + \nu_v \Delta_z \mathbf{u},\\
&\frac{\partial \theta}{\partial t} = \beta w + \kappa_h \Delta_h \theta + \kappa_v \Delta_z \theta,\\
&\nabla \cdot \mathbf{u} = 0.
\end{aligned} \tag{1}$$

In (1) $\mathbf{u}$ represents the velocity vector with w denoting its vertical component; ϕ is the normalized pressure perturbation from the reference state; g and α are, respectively, the acceleration of gravity and the coefficient of the volume expansion (here the reciprocal of reference potential temperature Θ_o); θ is potential temperature deviation from a linear profile with adverse gradient β; and subscripts $_h$ and $_v$ refer to the horizontal and vertical, respectively.

Taking twice the curl of the momentum equation in (1) results in the prognostic equation for the Laplacian of vertical velocity

$$\frac{\partial}{\partial t}\Delta w = g\alpha\Delta_h\theta + (\nu_h\Delta_h + \nu_v\Delta_z)\Delta w. \tag{2}$$

Postulating the solution in the form of Fourier modes

$$\begin{aligned}
&w = \hat{w}(z)\exp[i(k_x x + k_y y) + pt],\\
&\theta = \hat{\theta}(z)\exp[i(k_x x + k_y y) + pt]; \quad k^2 := k_x^2 + k_y^2, i := \sqrt{-1},
\end{aligned} \tag{3}$$

then substituting (3) in (2) and in the entropy equation in (1), and eliminating $\hat{\theta}$ from the two resulting equations yields

$$\left(\frac{d^2}{dz^2} - k^2\right)\left(\frac{\nu_v}{\nu_h}\frac{d^2}{dz^2} - k^2 - \frac{p}{\nu_h}\right)\left(\frac{\kappa_v}{\kappa_h}\frac{d^2}{dz^2} - k^2 - \frac{p}{\kappa_h}\right)\hat{w} = -\frac{k^2}{H^4}Ra_h\hat{w}, \tag{4}$$

where $Ra_h := \dfrac{g\alpha\beta H^4}{\nu_h\kappa_h}$ is the "horizontal" Rayleigh number. Because we are concerned with the convective response to numerical filters, we emphasize viscosity and diffusion in the horizontal rather than in the vertical (contrary to [43,44]), reflecting the anisotropy of grid resolution common in meso- and large-scale atmospheric models.

The marginal stability — that is, the transition between stable equilibrium and convective instability — occurs for $p = 0$, see Section 11 in [37].[5] With p set to zero, $\nu_h = \nu_v \equiv \nu$ and $\kappa_h = \kappa_v \equiv \kappa$, the relation (4) reproduces the classical vertical-structure equation

$$\left(\frac{d^2}{dz^2} - k^2\right)^3 \hat{w} = -\frac{k^2}{H^4}Ra\hat{w}. \tag{5}$$

An illustrative elementary case assumes free-slip impermeable flat boundaries in the vertical, implying $\hat{w} = (d^2/dz^2)\hat{w} = 0|_{z=(0,H)}$, and the resulting solution

$$\hat{w}(z) = A\sin\left(n\frac{\pi}{H}z\right), \tag{6}$$

which after inserting into (5) yields the marginal stability relation

$$Ra(k) = \frac{H^4}{k^2}\left(n^2\left(\frac{\pi}{H}\right)^2 + k^2\right)^3, \tag{7}$$

[5] A proof for anisotropic viscosity [48] closely follows that for the isotropic case, Chapter II.11 in [37].

alluded to earlier in Section 2.1. The implication of (7) is that for a given constant Rayleigh number $Ra = \mathscr{R}$, all horizontal modes k are unstable for which $Ra(k) < \mathscr{R}$. The critical Rayleigh number and the wavelength are defined by the minimum of (7) with respect to k at $n = 1$; see Section 15 in [37]. The critical wavelength and Rayleigh number are found as $\lambda_{cr} = 2\sqrt{2}H$ and $Ra_{cr} = 657.5$, respectively.

At $p = 0$, a range of effects due to the anisotropy of viscous forcings in (4) can be deduced from two asymptotic limits: $\nu_v/\nu_h \searrow 0$ together with $\kappa_v/\kappa_h \searrow 0$; and $\nu_v/\nu_h \nearrow \infty$ together with $\kappa_v/\kappa_h \nearrow \infty$. In the lower limit — representative of, say, $\nu_v = \kappa_v = 0$ — the vertical-structure Eq. (4) takes the familiar form of the oscillator equation

$$\frac{d^2}{dz^2}\hat{w} = -k^2\left(\frac{Ra_h}{H^4k^4} - 1\right)\hat{w}. \tag{8}$$

For $k^4 > Ra_h/H^4$, the solution is hyperbolic, and for the selected impermeable free-slip boundaries it must vanish identically (even as $H \nearrow \infty$). On the other hand, as $k^4 < Ra_h/H^4$ one can derive the marginal stability relation

$$Ra_h(k) = k^2H^2(k^2H^2 + n^2\pi^2), \tag{9}$$

which implies that the critical Rayleigh number is zero and that all modes longer than $2\pi H/Ra_h^{1/4}$ are convectively unstable.

In the upper limit — representative of, say, $\nu_h = \kappa_h = 0$ — the vertical-structure Eq. (4), after substituting (6), reduces to

$$Ra_v(k) = \pi^4\left(\frac{\pi^2}{k^2H^2} + 1\right), \tag{10}$$

where $Ra_v := \dfrac{g\alpha\beta H^4}{\nu_v\kappa_v}$. Relation (10) implies the stability of all modes for $Ra_v < \pi^4$, and otherwise the instability of all modes shorter than $2H\sqrt{\dfrac{Ra_v}{\pi^4} - 1}$.

The three asymptotic limits discussed above are illustrated in Fig. 3. In essence, the figure shows that decreasing ν_v, at constant ν_h, accentuates the instability of long modes, whereas decreasing ν_h, at constant ν_v, enhances the instability of short modes. These two extreme anisotropy cases will elucidate the effects of finite anisotropy discussed next.

Assuming isotropy of the Prandtl number $P_h = P_v = P$, substituting (6) into (4), defining the anisotropy ratio $r := \nu_v/\nu_h = \kappa_v/\kappa_h$ and manipulating the algebra leads to the marginal stability relation

$$Ra_h(k, r) = \frac{H^4}{k^2}\left(n^2\left(\frac{\pi}{\frac{H}{\sqrt{r}}}\right)^2 + k^2\right)^3 \frac{\left(n^2\left(\frac{\pi}{H}\right)^2 + k^2\right)}{\left(n^2\left(\frac{\pi}{H}\right)^2 r + k^2\right)}, \tag{11}$$

purposely written in a form similar to (7). To find the critical Rayleigh number for the instability onset, we evaluate the minimum of $Ra_h(k^2)$ at $n = 1$. The relation (11) has the minimum at

$$k_{cr}^2 = \frac{1}{4}\left(\frac{\pi}{H}\right)^2\left(\sqrt{8r + 1} - 1\right), \tag{12}$$

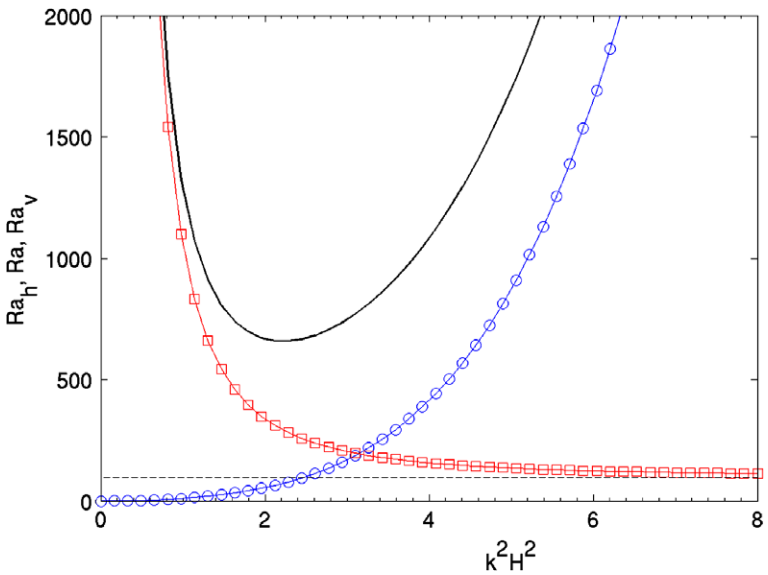

Fig. 3. Asymptotic marginal stability relations for $\nu_h = \nu_v$ (solid), $\nu_v = 0$ (circles) and $\nu_h = 0$ (squares) at a finite Prandtl number. Respective Rayleigh numbers Ra_h, Ra and Ra_v are shown as functions of the squared horizontal wave number (3). For each curve the stability region lies beneath.

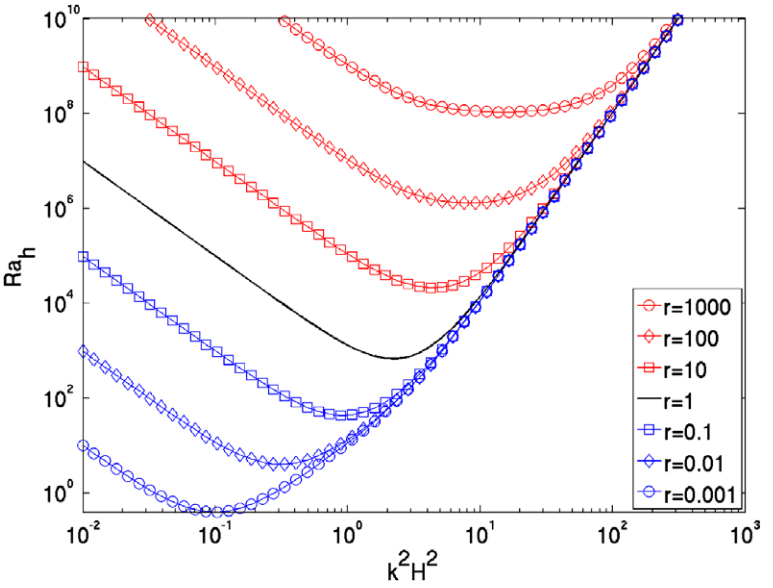

Fig. 4. Marginal stability relation (11) for finite anisotropy ratios $r = 10^{-3}, \ldots, 10^{3}$.

thus yielding

$$Ra_{h|cr} = \frac{\pi^4\left(\sqrt{8r+1}+3\right)\left(\sqrt{8r+1}-1+4r\right)^2}{16\left(\sqrt{8r+1}-1\right)}. \tag{13}$$

For $r = 1, 0$, and $r \nearrow \infty$, (13) reproduces the critical Rayleigh numbers of the marginal stability relations (7), (9) and (10), respectively. Moreover, for $Ra_h \gtrsim Ra_{h|cr}$, (12) implies the aspect ratio (squared) of dominant convective cells

$$\left(\frac{2H}{\lambda}\right)^2 = \frac{1}{4}\left(\sqrt{8r+1}-1\right). \tag{14}$$

Expanding (14) in the Taylor series about $r = 0$ gives $2H/\lambda = \sqrt{r}$, consistent with [44] and the Priestley's [41] scaling argument.

Fig. 4 illustrates (11) for a range of disperse values of the anisotropy ratio r at $n = 1$. It conveys that at a fixed value of Ra_h, the range of unstable horizontal modes diminishes with increasing anisotropy ratio r. Furthermore, Fig. 4 shows that as the anisotropy ratio increases, the critical Rayleigh number Ra_h increases monotonically; whereas the wavelength of the marginally stable mode diminishes gradually. The converse can be concluded for the analysis in terms of $Ra_v(k^2)$; cf. Fig. 8 in Section 3 of [44]. Notably, for sufficiently large (or small) k^2, the marginal stability expressed in terms of Ra_h (or Ra_v) is insensitive to r, reflecting the $k^2 \nearrow \infty$ and $k^2 \searrow 0$ limits of (11). However, for any given Rayleigh number exceeding the critical value (either in terms of Ra_h or Ra_v), the selection of modes and thus the organization of convection, depends significantly on r. This is substantiated by the results of 3D simulations and discussed in the remainder of the paper.

3. Numerical model

3.1. Analytic formulation

The nonhydrostatic model EULAG used in this study has been thoroughly documented in the literature; for a recent review see [26]. In general, EULAG admits a range of optional formulations of the equations of motion [49–51]. Here we are primarily concerned with idealized, nonrotating buoyancy-driven flows, whereupon we dispense with many capabilities (and complexities) of the model and simplify the presentation of the model formulation as well as of its computational procedures. The scope of this paper justifies a concise, operator-like symbolic description of the governing equations; for a thorough mathematical exposition of the governing equations refer to [52,53].

For the purpose of this study, we extend the compact form of the inviscid, adiabatic, anelastic equations of Lipps and Hemmler [54] to account for dissipative and diffusive effects

$$
\begin{aligned}
&\nabla\cdot(\rho_b\mathbf{v})=0,\\
&\frac{D\mathbf{v}}{Dt}=-\nabla\pi'-\mathbf{g}\frac{\theta'}{\theta_b}+\frac{1}{\rho_b}\nabla\cdot\boldsymbol{\tau},\\
&\frac{D\theta'}{Dt}=-\mathbf{v}\cdot\nabla\theta_a+\frac{1}{\rho_b}\nabla\cdot\mathscr{H},\\
&\frac{D\mathscr{E}}{Dt}=-\left(\boldsymbol{\tau}:\nabla\mathbf{v}+\frac{\mathbf{g}\cdot\mathscr{H}}{\theta_b}+\nabla\cdot\mathbf{T}+\varepsilon\right)\frac{1}{\rho_b}.
\end{aligned}
\tag{15}
$$

Here $D/Dt=\partial/\partial t+\mathbf{v}\cdot\nabla$; $\mathbf{v}$ denotes the velocity vector; θ, ρ, and π refer to potential temperature, density, and a density-normalized pressure, respectively; and $\mathbf{g}$ is the vector of gravitational acceleration. Primes denote deviations from the ambient state. The subscript $_b$ refers to the basic state, i.e., a horizontally homogeneous hydrostatic reference state of the Boussinesq expansion around a constant stability profile (see Section 2b in [55], for a discussion). The divergence terms on the rhs of the second and the third equation represent dissipation of momentum and diffusion of heat, respectively. The deviatoric stress tensor is $\boldsymbol{\tau}=2\rho_b\nu_e[\mathscr{D}-(1/3)\mathrm{tr}(\mathscr{D})\mathscr{I}]$, and the heat flux is $\mathscr{H}=\rho_b\kappa_e\nabla\theta$; the deformation tensor is $\mathscr{D}=0.5(\nabla\mathbf{v}+\nabla\mathbf{v}^T)$, and $\mathscr{I}$ denotes the identity matrix. The corresponding eddy coefficients are proportional to the square root of the "turbulent kinetic energy" $\mathscr{E}$. The evolution of $\mathscr{E}$ in (15) outlines the standard prognostic "TKE" subgrid-scale model, with the rhs forcings accounting for shear and heat production, turbulent transfer and dissipation [56,57]. The latter two terms are parameterized assuming $\mathbf{T}\propto\nu_e\nabla\mathscr{E}$ and $\varepsilon\propto\delta_e\mathscr{E}^{3/2}$, with δ_e denoting the mixing length (a measure of grid resolution, tapered where approaching the wall boundaries). Notably, neglecting the advective transport on the lhs and the turbulent transfer on the rhs leads to the classical diagnostic Smagorinsky-type model with eddy-viscosity $\propto\delta_e^2\|\mathscr{D}\|_F$; for further discussion see [56,57] and references therein. In calculations with arbitrarily prescribed eddy coefficients the prognostic TKE equation is dismissed.

3.2. Numerical approximations

In EULAG all governing prognostic equations can be optionally integrated as either Lagrangian evolution equations or Eulerian conservation laws, both cast in generalized time-dependent coordinates enabling grid adaptation to irregular model domains or flow features [26]. All calculations reported in this paper used the Eulerian Cartesian-framework formulation exclusively. Given the mass continuity equation, each prognostic equation in (15) is idealized as

$$
\frac{\partial\rho_b\Psi}{\partial t}+\nabla\cdot(\rho_b\mathbf{v}\Psi)=\rho_b F,
\tag{16}
$$

where Ψ symbolizes components of $\mathbf{v}$ as well as θ' or $\mathscr{E}$, and F denotes the associated rhs in (15). The governing system of the conservation laws (16) is integrated numerically using a second-order-accurate, semi-implicit, non-oscillatory forward-in-time (NFT) approach, whose theory, implementation and applications are broadly documented in [28,51,58] and references therein. All prognostic dependent model variables are co-located — a choice important for the efficacy of the semi-implicit integrals (cf. [59]) — so the resulting finite-difference approximations can be written compactly as

$$
\Psi_{\mathbf{i}}^{n+1}=\mathscr{A}_{\mathbf{i}}(\widetilde{\Psi},\mathbf{v}^{n+1/2},\rho_b)+0.5\Delta t F_{\mathbf{i}}^{n+1}.
\tag{17}
$$

Here $\Psi_{\mathbf{i}}^{n+1}$ is the solution sought at the grid point $(t^{n+1},\mathbf{x}_{\mathbf{i}})$, $\widetilde{\Psi}_{\mathbf{i}}\equiv\Psi_{\mathbf{i}}^{n}+0.5\Delta t F_{\mathbf{i}}^{n}$, $\mathbf{v}^{n+1/2}$ is an $\mathscr{O}(\Delta t^2)$ estimate of the velocity at $t+0.5\Delta t$, and $\mathscr{A}$ denotes a fully second-order-accurate two-time-level finite-volume NFT advection scheme. All calculations in this paper used the second-order-accurate monotone MPDATA scheme; already widely reviewed in the literature [28,29,51].

For inviscid dynamics, all prognostic equations in (15) are integrated with (17) using, effectively, the trapezoidal rule and thus treating all forcings on the right-hand side implicitly. Viscous terms in the momentum and the entropy equation (and the combined forcings of the TKE model) are evaluated explicitly to $\mathscr{O}(\Delta t)$, and are included in $\mathscr{A}$. This is arguably justified, because they enter the equations of motion via the subgrid-scale (SGS) model as $\sim\mathscr{O}(\delta_e^2)$ corrections. In technical terms, the definition of the auxiliary field $\widetilde{\Psi}$ is expanded as $\widetilde{\Psi}\equiv\Psi^n+0.5\Delta t(F_{rsv}^n+2F_{sgs}^n)$, while accounting only for the resolved forcing F_{rsv} in F^{n+1} on the rhs of (17);[6] see Sections 3.5.4 and 4.2 in [28] for further discussion. The explicit first-order evaluation of SGS forcings improves the efficacy of the calculations; however, when required, it can be extended to a trapezoidal integration by means of an outer iteration scheme [51,60]. The semi-implicit formulation underlying the NFT template algorithm (17) leads to a complicated elliptic problem for pressure (cf. Appendix A in [52], for the complete description), which is solved iteratively using the preconditioned generalized conjugate-residual approach, a non-symmetric Krylov-subspace solver. For recent succinct reviews of the complete model numerics in diverse atmospheric and oceanic applications, the interested reader is referred to [51,59,61]. For examples of benchmark simulations underlining the veracity of the EULAG model see [62,63].

Integrating the governing PDE as described has two important benefits relevant to this study. First, transporting only perturbations of potential temperature, while retaining the convective derivative of the background state on the rhs, assures conservation of θ' with accuracy to round-off error (Section 3a in [49]) tantamount to preventing dilution of the background stratification due to the implicit viscosity of non-oscillatory advection. Second, among non-oscillatory schemes, MPDATA appears to have unique dissipative properties [64] in mimicking the action of explicit subgrid-scale turbulence models where the flow is under-resolved [57,58,65–67]. In particular, the effective viscosity of MPDATA is adaptive — i.e., the correspond-

[6] By definition, $F_{rsv}\equiv 0$ in the evolution equation for $\mathscr{E}$ in (15), thus resulting in the Euler-forward integral of the underlying ODE; cf. Eqs. (24) and (25) in [51] and the accompanying discussion.

ing dissipation rate decreases with increasing explicit viscosity [68] — making MPDATA methods suitable for direct numerical simulation (DNS) and large-eddy simulation (LES) as well as for implicit LES (ILES) [69]. Altogether, this facilitates a variety of discriminating numerical experiments addressing the role of explicit/implicit viscosity, and of the effective Rayleigh number, in the development of coherent structures in simulated convective fields.

4. Reference simulation

4.1. Setup

The reference simulation specified in this section represents a hypothetical high-resolution prediction of mesoscale weather. Global models with horizontal grid spacing $\Delta_H \approx 10$ km are already entering the realm of NWP [10,70], thus paving

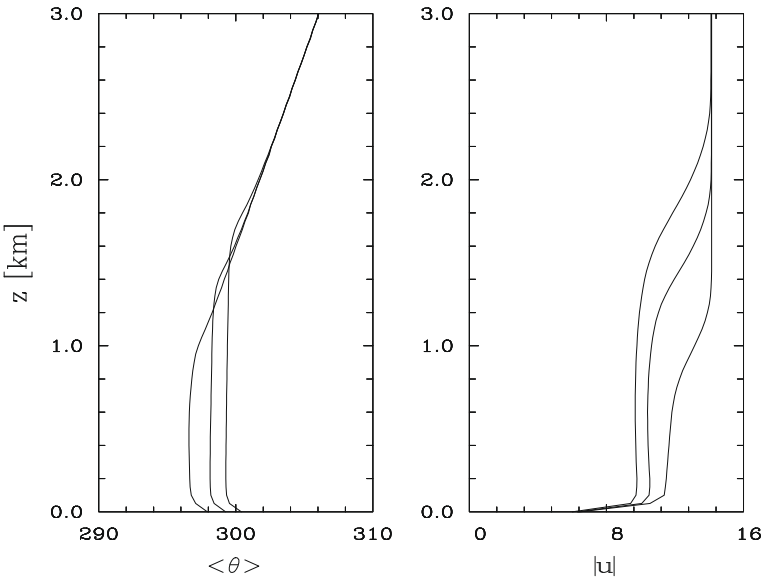

Fig. 5. Reference simulation: profiles of horizontally averaged field of potential temperature θ and horizontal wind speed $\sqrt{u^2+v^2}$ at $t = 2,\ 4$, and 6 h.

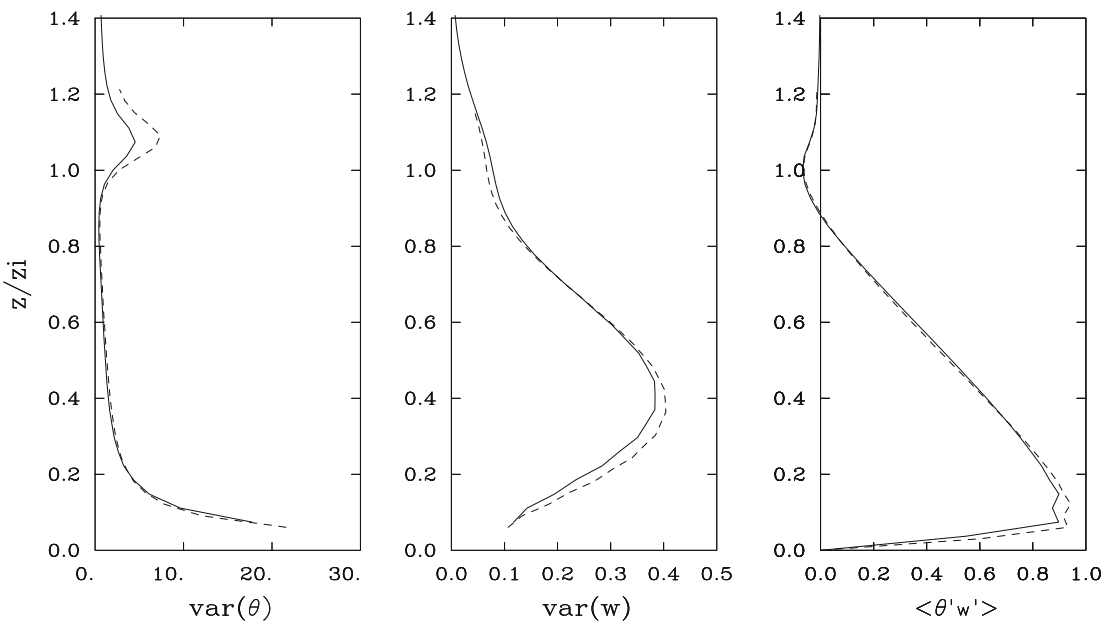

Fig. 6. Dimensionless profiles of temperature and vertical velocity variance (left and center) and of turbulent heat flux (right), at $t = 4$ (solid) and 6 h (dashed).

the way for equally intensive calculations at smaller scales. A $\Delta_H \approx 10$ km global simulation translates to a regional/mesoscale NWP with 20 times higher resolution $\Delta_H \sim 0.5$ km. Here, we consider the minimal model of fair weather by simulating dry thermal convection over a flat plane. The model domain is 9 km in the vertical and 64×64 km^2 in the horizontal. The adopted domain size in each horizontal direction exceeds the scale of observed fair-weather convective structures by many times [71]. The vertical extend of the domain accommodates one wavelength of the dominant hydrostatic gravity wave. The ambient potential temperature profile is specified in terms of stratification S as $\theta_a(z) \equiv \theta_b(z) = \theta_o \exp(Sz)$, with assumed surface value $\theta_o = 293.15$ K and buoyancy frequency $N = (gS)^{1/2} = 0.012$ s^{-1}. The uniform ambient wind $\mathbf{v}_a = [-10, -10, 0]$ ms^{-1} is directed from the north-east. Convection is driven by constant surface heat flux $H_o = 0.2$ K ms^{-1} (representative of mid-latitudes) distributed vertically in the vicinity of the lower boundary by means of subgrid-scale fluxes evaluated with the standard TKE turbulence model [56,57] where Prandtl number $P = 0.42$ is assumed. Rotational effects are neglected in all simulations discussed in this paper.

The model domain is resolved with $nx \times ny \times nz = 127 \times 127 \times 180$ uniform grid intervals $\Delta x = \Delta y \approx 500$ m and $\Delta z = 50$ m, respectively. The simulation is carried out for $t = 6$ h of physical time, using a constant time step $\Delta t = 5$ s. The effective Courant number $\mathscr{C} = \max \sum \Delta t |u^I| / \Delta X^I \approx 0.7$ is used throughout the simulation; here the summation is over $I = 1, 2, 3$, corresponding to

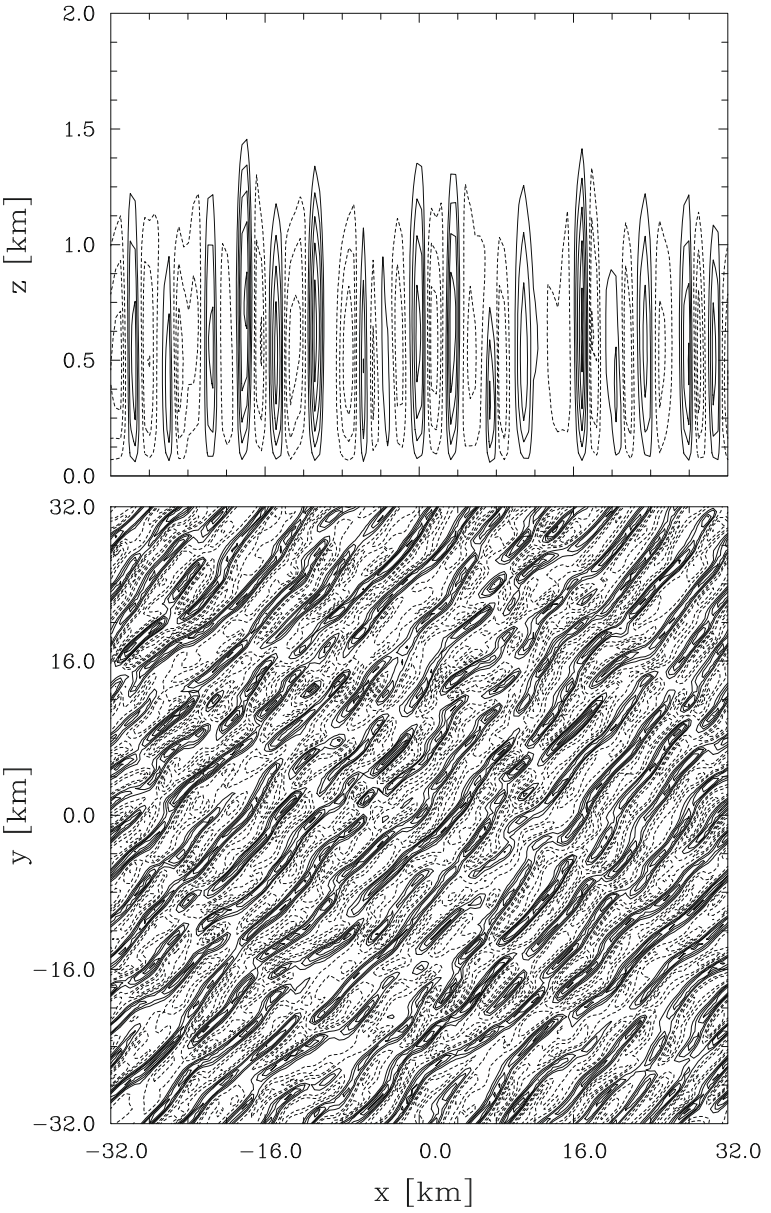

Fig. 7. Reference simulation: contours of vertical velocity in central xz plane (top) and in the xy plane at $z = 450$ m (bottom) at $t = 4$ h of the simulated time. The contour interval is 0.5 ms^{-1} in both panels; solid/dashed lines are for positive/negative field values, and zero contour lines are not shown.

three orthogonal directions x, y and z, while the maximum is taken over the entire model domain. The boundary conditions are periodic in the horizontal. In the vertical, the lower boundary is impermeable with partial slip modeled by the standard drag law for the surface stress components $\tau_{l3} = C_d \|\mathbf{v}\| v^l|_{l=x,y}$, and assuming a drag coefficient $C_d = 0.01$. The upper boundary is impermeable free-slip, decoupled from the interior of the domain by means of a 2 km deep sponge layer. The initial conditions consist of the ambient flow, with a small-magnitude white noise imposed on the flow and temperature field.

4.2. Results

The results of the reference experiment are summarized in Figs. 5–7. Fig. 5 shows vertical profiles of the horizontally averaged fields of potential temperature $\langle\theta\rangle(t,z)$ and horizontal wind speed $\langle(u^2+v^2)^{1/2}\rangle(t,z)$, after 2, 4 and 6 h of the simulated time. The simulated convective planetary boundary layer (PBL) grows roughly as $\sqrt{Kt}$, with $K \approx 120$ m^2 s^{-1}, reaching heights of 800, 1350 and 1650 m after 2, 4 and 6 h, respectively. Fig. 6 shows three normalized second-order moments at $t = 4$ and 6 h when the PBL is already developed and its depth well resolved. The moments shown are the variances of potential temperature $\langle(\theta'/T^*)^2\rangle$ and of vertical velocity $\langle(w'/w^*)^2\rangle$, and the resolved heat flux $\langle(\theta'/T^*)(w'/w^*)\rangle$. Here primes refer to deviations from horizontal averages, and $w^* = (g/\Theta_o z_i H_o)^{1/3}$ with z_i denoting the PBL height defined by the minimum of the total (horizontally averaged) heat flux. For consistency, a convective temperature scale is defined as $T^* = H_o/w^*$. Note that the horizontal resolution employed is one order of magnitude coarser than those typically used in focused LES studies of

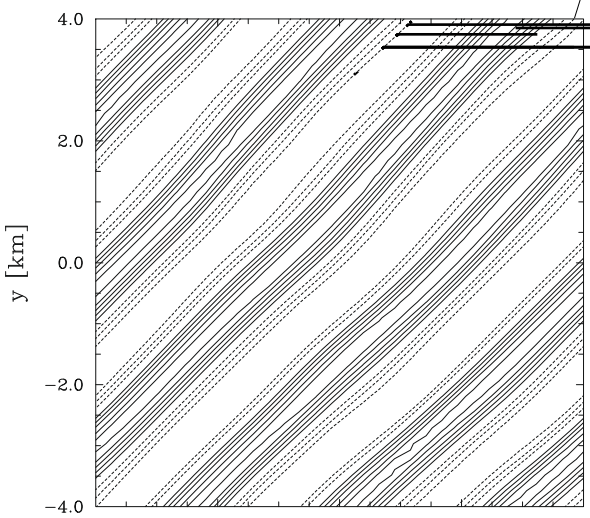

which statistical algorithms are modeled [72]. Supplementary quantitative evidence is provided in Section 5.1 where LES convergence is illustrated with power spectra; cf. [58,65] for discussions.

Fig. 8 shows the vertical-velocity field at the time and height of Fig. 7. The horizontal grid interval decreases from about 250 m in the upper-left panel, through 125 and 62 m in the upper-right and lower-left panels, to 31 m in the lower-right panel. The $\Delta_H = 250$ m result closely resembles the roll organization in Fig. 7 even though it uses nearly twice the resolution in all three directions. At $\Delta_H = 125$ m, a breakup of the coherent roll organization is apparent; whereas both fine-resolution simulations seem to favor a more cellular-type organization of convective elements. Note that at the 31.25 m grid interval the spanwise width of updrafts is already resolved with 10–20 grid points.

Fig. 9 extends the sequence of results in Fig. 8 to a finer horizontal resolution of $\Delta_H \approx 15$ m, while reducing the horizontal domain. The two upper panels corroborate the finest result of Fig. 8, in the sense that at horizontal scales of $\mathcal{O}(10^3)$ m, they still reveal elements of cellular organization. Consistent with the finite scale of convection organization implied by Fig. 8, as the linear size of the domain decreases below 2 km, the two lower panels in Fig. 9 show a random updraft/downdraft pattern without a trace of organization. It is noteworthy that all four panels predict the width of the updraft patterns at $\mathcal{O}(10^2)$ m, which is consistent with the range of values depicted in the lower-right panel of Fig. 8.

The structural convergence analysis highlighted in Figs. 8 and 9 illustrates the thesis that capturing the realism of PBL convection requires horizontal domains of $\mathcal{O}(10) \times \mathcal{O}(10)$ km^2 resolved with $\mathcal{O}(10) \times \mathcal{O}(10)$ m^2 grid intervals. In simulations of meso- to regional-scale weather and climate, the required resolutions may be thus computationally unaffordable in routine calculations for quite a while, despite the rapid progress in computer technology. Consequently, the quality of the solution shown in Fig. 7 appears representative of the high-resolution results attainable with modern meso- to regional-scale

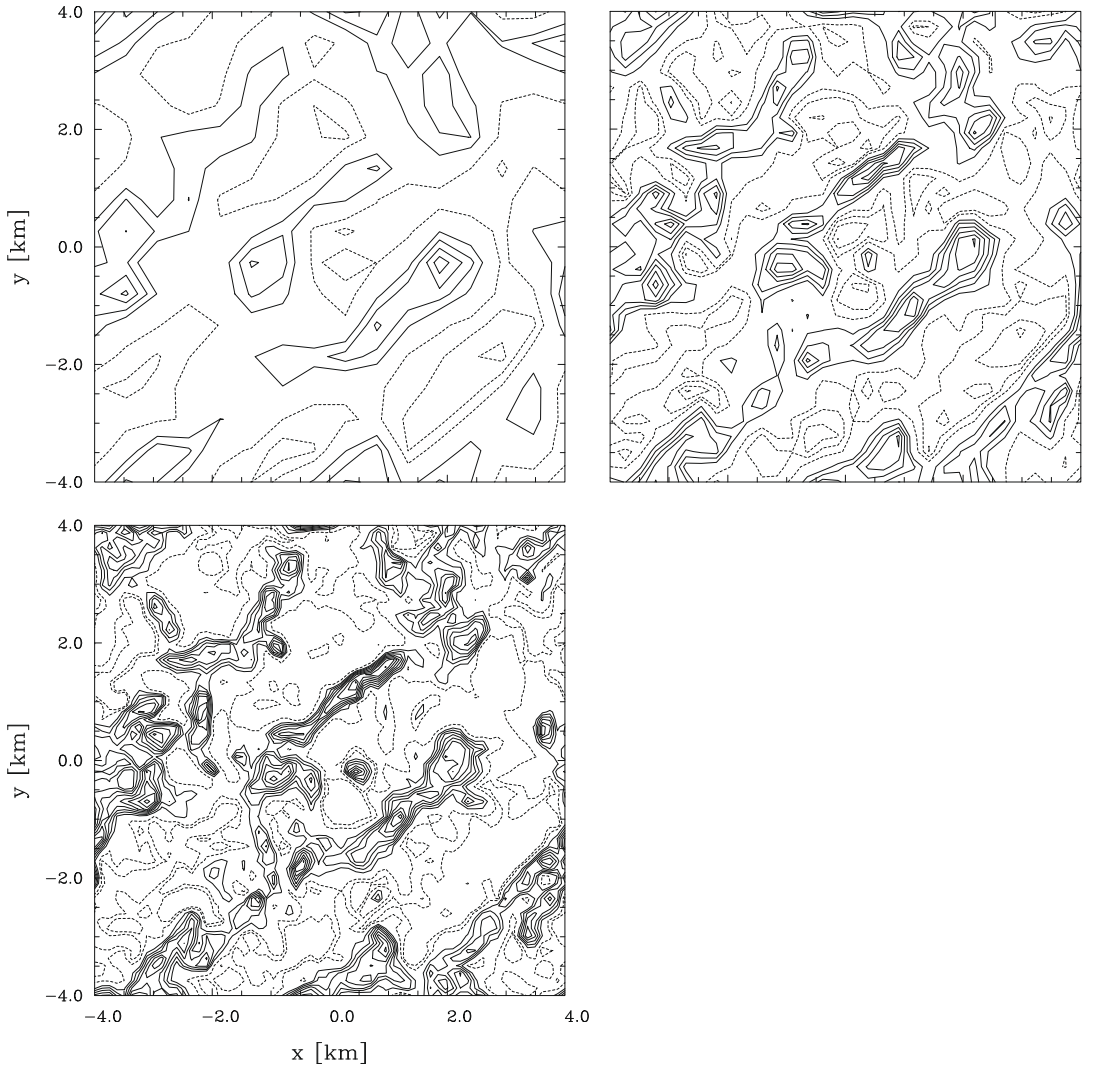

simulations. Even though the results in Fig. 7 depart visibly from the finely resolved field (e.g. the lower-right panel of Fig. 8) in principle, they may still capture the correct solution in a mean sense. In particular, given an effective subgrid-scale model, the under-resolved result in Fig. 7 may accurately represent the finely-resolved solution averaged to the coarse model grid. Fig. 10, however, shows that this is not the case. The coarsened fields convey the signature of the cellular structure of the finely resolved field throughout all levels of coarsening, and none of them resemble any of the three coarsely resolved results in Fig. 8. In other words, the reference result in Fig. 7 does not adequately capture the structure of finely resolved PBL convection (modulo filter of the employed subgrid-scale model).

5. Effects of numerical truncation

5.1. Implicit large-eddy-simulation

The lack of correspondence between the coarsely resolved and coarsened finely-resolved results in Figs. 8 and 10, respectively, puts in doubt the physical significance of the simulated convective structures, leaving the estimated moments'

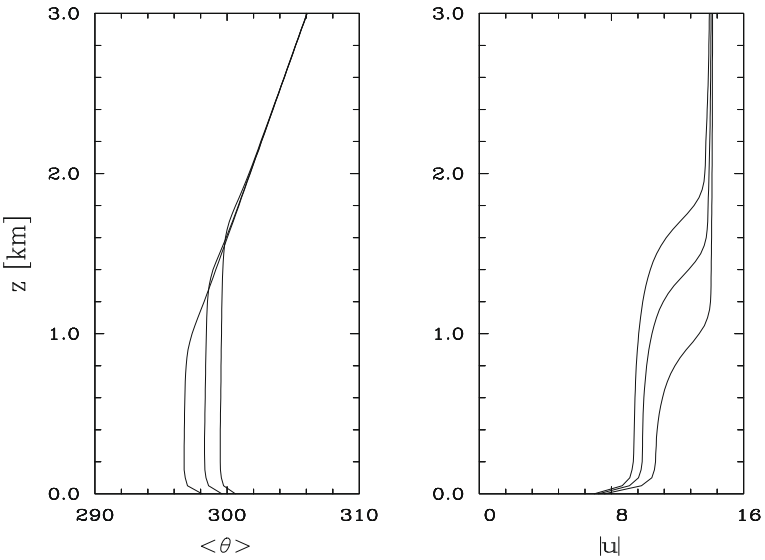

Fig. 11. Profiles of temperature and wind speed as in Fig. 5 but for ILES.

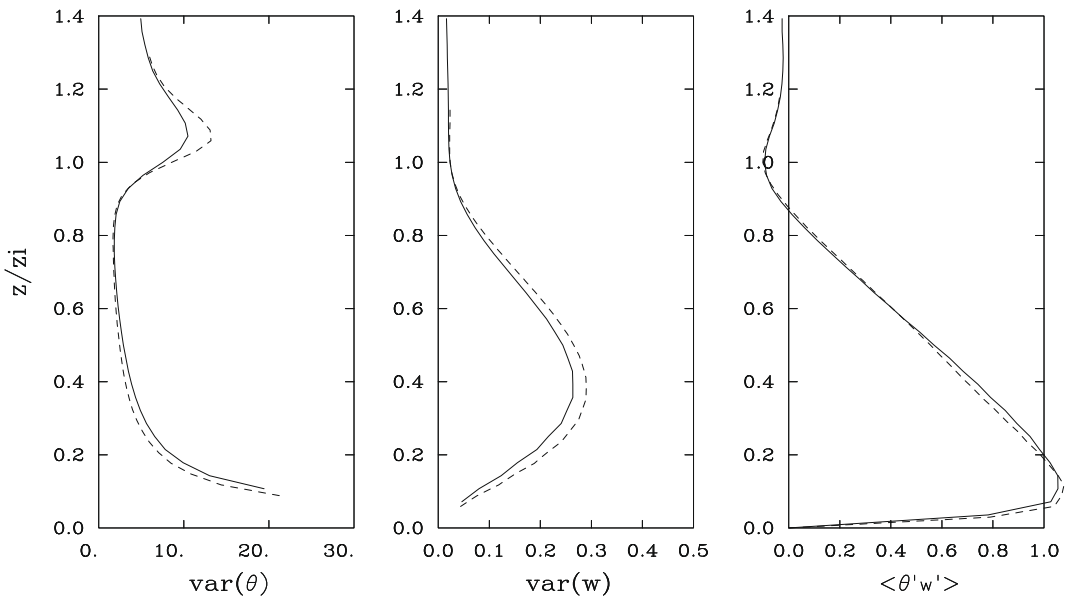

Fig. 12. Profiles of temperature and vertical velocity variance and of turbulent heat flux, as in Fig. 6 but for ILES.

profiles perhaps the only useful outcome of such challenging yet under-resolved computational efforts. Notably, a similar study [73], which used this same numerical model set for a synoptic-scale orographic flow, showed quite a contrasting result with close correspondence between coarse and coarsened solutions; see their Figs. 14 and 15 and the accompanying discussion. While a more linear flow response in [73] may play a role in explaining this discrepancy, another factor worth consideration is a minimized effective viscosity due to the implicit large-eddy-simulation (ILES) approach employed in their study. ILES dispenses with explicit subgrid-scale models and exploits truncation properties of high-resolution (non-oscillatory) finite-volume methods to mimic the spectral viscosity of standard LES [66,67,74]. This minimizes the computational effort while maximizing the effective Reynolds number of simulations [63]. In the following, we compare the ILES with the reference LES discussed in Sections 4.2 and 4.3. The ILES experiment is set in the same manner as the LES described in Section 4.1, except that it dismisses the viscous terms and the turbulent kinetic energy equation in (15). To distribute heat and momentum in the vicinity of the lower boundary, the minimal analytic wall model is prescribed in (15), in the spirit of [57]. For the heat- and momentum-flux profiles, $h(z) = H_o \exp(-0.02z)$ and $q^l(z) = -C_d^* \|\mathbf{v}_{(z=0)}\| v^l_{(z=0)} \exp(-0.02z)|_{l=1,2}$ are assumed; the (negative) vertical derivatives of which enter on the rhs of the entropy and horizontal momentum equations, respectively. The results are only weakly sensitive to the assumed $\mathcal{O}(\Delta z)$ value of the vertical attenuation scale in the minimal models.

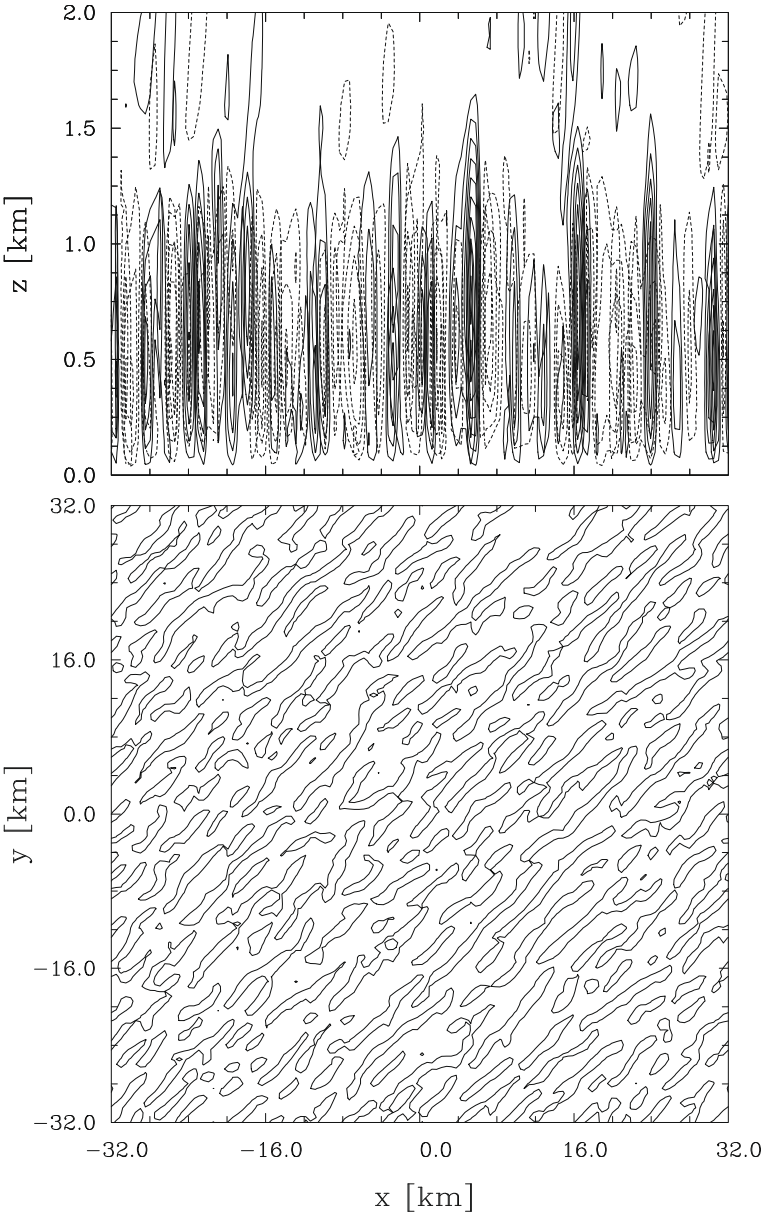

Figs. 11–13 show the ILES results, corresponding to the LES solution in Figs. 5–7. Overall, the two solutions are in a qualitative agreement. Some discrepancy in the second-order moments can be attributed to the Prandtl number effect enhancing diffusion of heat, compared to the momentum dissipation, in the LES case; formally, $P = 1$ in ILES. Notably, using a slightly more diffusive version of MPDATA for integrating the entropy equation recovers the variance of w from LES. To compensate (somewhat) for this deficiency of ILES while retaining the same numerics in both series of experiments, the drag coefficient $C_d^* = 0.5C_d$ was used. The discrepancy in the instantaneous w fields in Figs. 7 and 13 is indicative of smaller effective viscosity of ILES. Note the evidence of the PBL-induced gravity wave activity aloft [75] in the upper panel of Fig. 13 and the more random character of the convective structures in the lower panel consistent with the enhancement of short horizontal scales apparent in the ILES result. The observed discrepancies diminish as the model resolution increases (not shown), and they could be minimized with a fine tuning of the two simulations. However, they are immaterial insofar as the following discussion and the theses of this work are concerned.

Figs. 14 and 15 highlight the structural convergence analysis respective to that in Figs. 9 and 10. An overall impression is that ILES evinces a somewhat higher effective resolution than LES. In both cases cellular organization appears to emerge at fine resolutions, yet in the ILES it appears to emerge from a more chaotic state. Consistently, the coarsening in Fig. 15 of the finest result of Fig. 14 verifies better structural character of the coarsely resolved calculations in Fig. 15, consonant with the spectral analysis in Fig. 16. That is, the NFT numerics of ILES capture the effect of unresolved scales of motion on the resolved scales better than the explicit subgrid-scale model of the LES; or, alternatively, the under-resolved LES solution is obscured by moderate Rayleigh number effects discussed in Section 2. Ultimately, the purpose of this work is not to argue in favor of either approach, but to use both approaches as convenient tools for investigating the sensitivity of convection reliability in

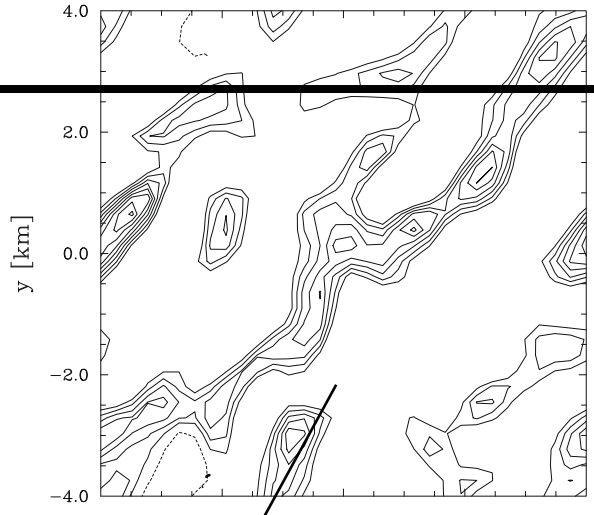

numerical models to either explicit or implicit filtering unavoidable (practically) in under-resolved simulations of multi-scale weather phenomena [9].

5.2. Numerical artifacts

To shed light on the different structural behavior of thermal convection already noted in the under-resolved LES and ILES calculations, here we summarize a series of controlled experiments addressing the impact of effective viscosity on the organization of the simulated convective boundary layer. The series consists of numerous simulations varying the numerical and physical setups. The numerical setups include modifications to advection schemes (from altering the limiters or the magnitude of antidiffusive fluxes in MPDATA, to replacing MPDATA with an Adams–Bashforth scheme), different realizations of explicit viscosity as well as its anisotropy and distribution between the momentum and temperature equations, and different flow alignment with the grid (via varying wind direction) — many at a range of horizontal resolutions. The various physical setups account for different wind magnitudes (including zero ambient flow), inclusion of the Coriolis force and the diurnal cycle, and a range of vertical boundary conditions testing sensitivity to the model depth and to the rate of momentum sink at the lower surface. Below we summarize selected key results; the comprehensive presentation of the series of simulations will be given in [48].

The numerical experience gained from the sensitivity studies documents that for horizontally under-resolved simulations there is a direct connection between anisotropy of the model effective viscosity and the occurrence of cellular structures.

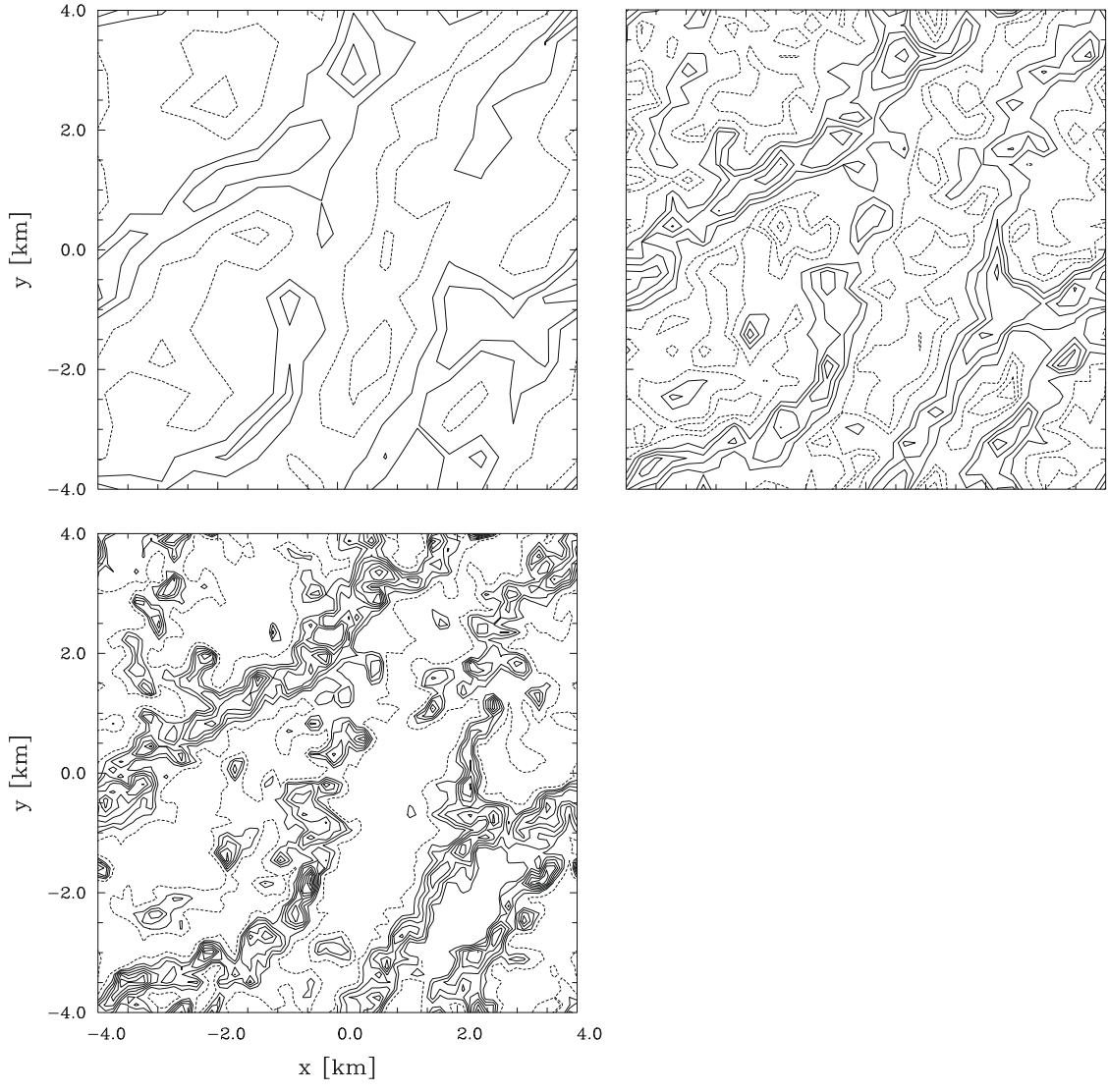

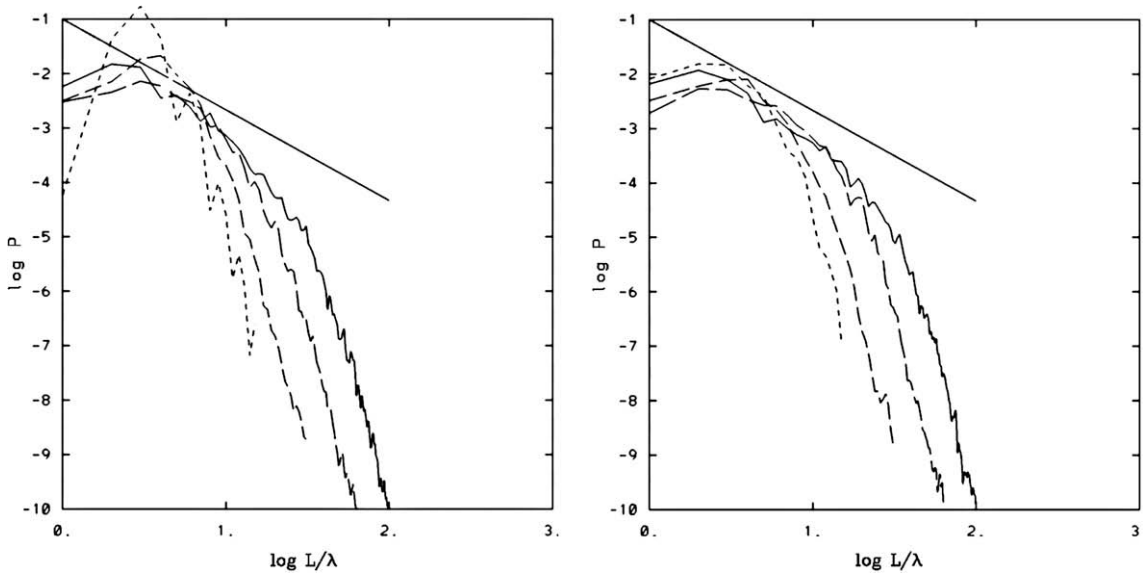

Fig. 16. Diagonal ($k_x = k_y$) of the 2D power spectra P of vertical velocity at different Δ_H; left and right panels correspond to Figs. 8 and 14, respectively. The "−5/3" slope is shown for reference.

Furthermore, the resulting structures appear consistent with the linear theoretical estimates, thus documenting the importance of moderate Rayleigh number effects in virtual reality of under-resolved simulations. Consequently, the specifics of realizing the anisotropic effective viscosity in computational models are, essentially, irrelevant. Fig. 17 and the accompanying discussion illustrate these conclusions.

The upper left plate in Fig. 17 shows the solution equivalent to that in the bottom plate of Fig. 13, except for the use of a dissipative filter intrinsic to composite schemes [30,31]. The original idea was to exploit the design of the classical two-step Lax–Wendroff scheme such as to rely on the dissipative Lax predictor by skipping the dispersive leap-frog corrector every $\mathscr{N}$th time step. The concept is attractive as it reduces the computational complexity, and readily extends to a variety of high-resolution schemes such as MPDATA, FCT, and even limited one-step algorithms. The solution in the upper left plate applies the generic first-order-accurate upwind (without the MPDATA antidiffusive correction) every 4th time step. It has been verified that the form of the filter is not fundamental, as a close result can be obtained by admitting a fourth of the dissipation at every time step. The latter can be realized in a number of ways, from reducing accordingly (here by a quarter) the magnitude of antidiffusive compensation in MPDATA to introducing explicit filters with equivalent effective dissipation. Because the implicit viscosity of the first-order upwind scheme $\kappa^l \sim 0.5(|u^l|\Delta x - (u^l)^2\Delta t)$ is well known [28,29,51], it is easy to estimate its magnitude. Retrieving mean u and v velocity components ≈ 7 m/s from the profiles (cf. Figs. 5 and 11) and taking horizontal and temporal grid increments of 500 m and 5 s, respectively, and then dividing the resulting κ^l by $\mathscr{N} = 4$, gives the effective horizontal viscosity $\nu_h = 425$ m^2 s^{-1}. Retrieving the vertical velocity component is more problematic, as its mean vanishes to the round-off error controlled by the specified accuracy of the elliptic solver. However, the variance of the w profile is observed at ≈ 0.7 m^2 s^{-2}, resulting in the effective $\nu_v \approx 2.5$ m^2 s^{-1} estimate consistent with eddy-viscosity profiles (not shown) for the TKE reference run discussed in Section 4.2. In contrast to the horizontal entry, the actual magnitude of the effective ν_v is subject to larger relative variations from case to case and may affect the details of simulated convective structures. However, because it is two orders of magnitude smaller than its horizontal counterpart, its uncertainty appears insignificant.

The remaining two contour plots in Fig. 17 employ: (i) ILES with the "1–2–1" low pass spatial filter every 30th time step, corresponding to the constant-coefficient horizontal diffusion with $\nu_h = (1/30) \cdot (0.25\Delta x^2/\Delta t)$; and (ii) explicit diffusion with constant anisotropic viscosity coefficients $\nu_h = 425$ m^2 s^{-1} and $\nu_v = 2.5$ m^2 s^{-1}. Notably, calculations with equal $\nu_h = \nu_v = 2.5$ m^2 s^{-1} throughout produce results similar to those with ILES in Fig. 13. This shows the insignificant filtering effect at such small values, except for providing a means to vertically distribute heat and momentum in the vicinity of the lower surface of the model.

In general, the problem of pattern selection for Rayleigh–Bénard convection is complicated [19], and interpreting the results of Fig. 17 in terms of the linear theory in Section 2.2 can be quite involved. However, some elementary bounds of geometric characteristics are straightforwardly deducible from the simulation parameters and results. For instance, the meaningful wavelengths $5\Delta x \lesssim \lambda < 127\Delta x$ are restricted by the domain size and marginal resolution, yielding $0.1 < k < 2.5$ km^{-1}, consistent with the spectra in Fig. 17. Inspection of the profiles gives an estimate of the effective Rayleigh number $Ra_h \simeq 77$ — assuming $\nu_h = 425$ m^2 s^{-1}, $P = 0.42$, $\Delta T = 1$K, $T_0 = 298$ K and $H = 1$ km. For the anisotropy ratio $r = 1/170$ the intersection of the marginal stability relation (11) with $Ra_h \simeq 77$ implies the unstable mode range $0.02 < k < 2.24$ km^{-1}.

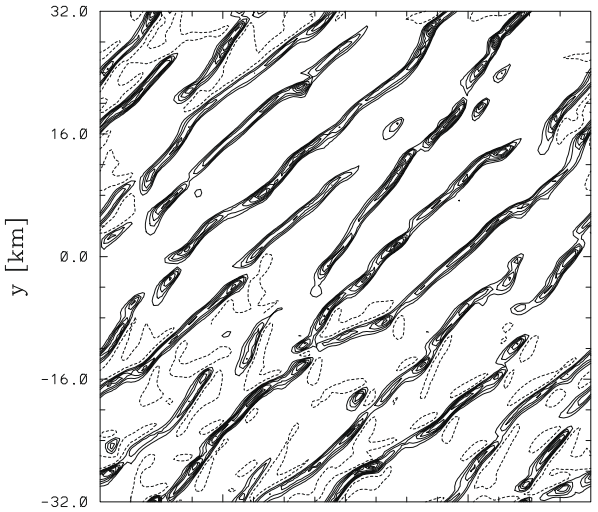

In order to quantify the characteristic separation scales of the elongated structures seen in Fig. 17, we examine the displayed w fields against their second-order structure function

$$g(\delta x, \delta y) = \frac{1}{nx \cdot ny} \Sigma_{i=1}^{nx} \Sigma_{j=1}^{ny} [w(x_i + \delta x, y_j + \delta y) - w(x_i, y_j)]^2, \tag{18}$$

and the corresponding autocorrelation function

$$a(\delta x, \delta y) = \frac{1}{\sigma^2} \Sigma_{i=1}^{nx} \Sigma_{j=1}^{ny} [w(x_i + \delta x, y_j + \delta y) - \bar{w}][w(x_i, y_j) - \bar{w}], \tag{19}$$

where overbar denotes the horizontal mean, and $(\delta x, \delta y)$ is the translation vector. Fig. 18 shows normal to the mean wind cross-sections of 2D functions (18) and (19), for the solution shown in the lower-left panel of Fig. 17. The first corresponding minimum and maximum of the two functions (and thus the shortest characteristic separation distance of either updraft or downdraft patterns) appears at about 5 km, or equivalently $k \approx 1.3$ km^{-1}, seen also in the updraft patterns in Fig. 17. The accentuated pairs of the extrema also appear at the separation scales of about 10, 22 and 27 km, all identifiable in the corresponding w display. These values are not exclusive to the selected panel but are representative of all three xy cross-sections of w fields in Fig. 17.

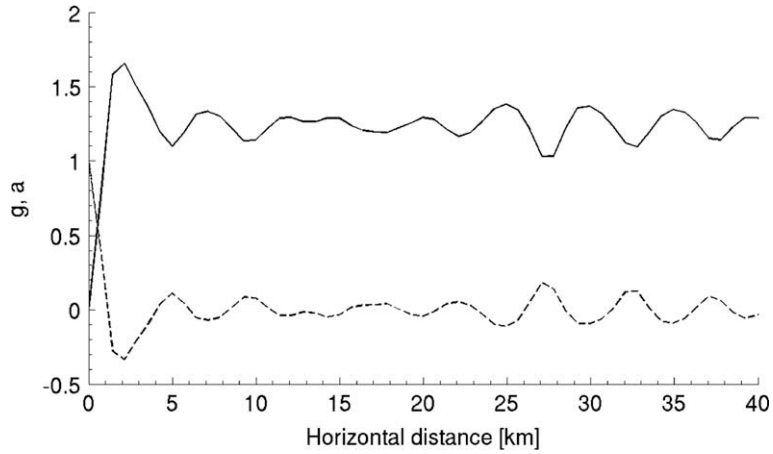

Fig. 18. Normal to mean wind cross-section of the second-order structure function (solid) and the autocorrelation function (dashed) of the w field in the lower-left panel of Fig. 17.

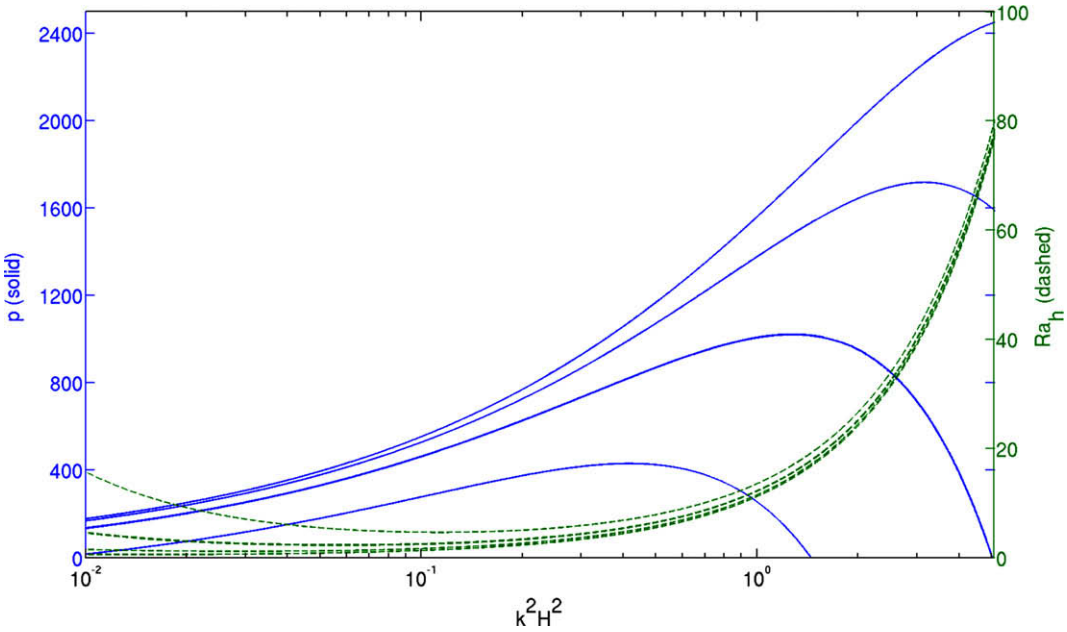

Fig. 19. Growth rate curves $p_1(k^2)$ (solid) and marginal stability curves $R_c(k^2)$ (dashed) for the most unstable vertical mode $n = 1$; the two slightly thicker curves correspond to the solutions in Fig. 17 with $r = r_o = 1/170$, whereas the remaining curves are for $r = 0.5r_o,\ 2r_o,\ 4r_o$ while keeping ν_v fixed.

The 27 km mode observed in Figs. 17 and 18 is consistent with the critical mode $k_{cr} = 0.24\ \mathrm{km}^{-1}$, specified in (12) and located at the minimum of the thicker dashed curve $R_c(k^2)$ in (Fig. 19). For $r = 1/170$ the critical value $Ra_{h|cr} \approx 2$ in (13) is much smaller than the effective $Ra_h \simeq 77$ of the experiments discussed. In consequence, the band of unstable modes $(0.02 < k < 2.24\ \mathrm{km}^{-1})$ obscures the critical mode, complicating the canonical linear prediction for a $Ra_h \gtrsim Ra_{h|cr}$ region of the solution space near marginal stability. To examine the linear theory prediction for the unstable modes, (4) is solved for the vertical mode (6) while admitting $p_n \neq 0$. The determinant of the resulting dispersion relationship

$$\frac{p_n^2}{\nu_h k_h} + \frac{p_n}{\nu_h \kappa_h}\left(r\frac{\pi^2 n^2}{H^2} + k^2\right)(\nu_h + \kappa_h) + \left(r\frac{\pi^2 n^2}{H^2} + k^2\right)^2 - \frac{Ra_h \cdot k^2}{H^4}\left(\frac{\pi^2 n^2}{H^2} + k^2\right)^{-1} = 0, \tag{20}$$

is always positive, which ensures two real solutions for p

$$p_n^{\pm} = \frac{\nu_v}{2P}\left(\frac{\pi^2 n^2}{H^2} + \frac{k^2}{r}\right)\left(-(P+1) \pm \sqrt{(1-P)^2 + 4Ra_v P \frac{r^2}{Ra_h|_{(11)}}}\right) \tag{21}$$

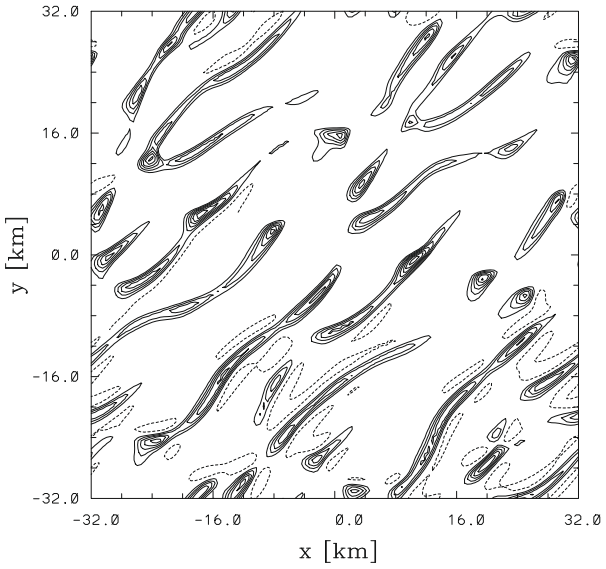

one of which is always negative, thus representing the decaying modes that are of no concern. The notation in (21) has been contracted compared to (20), to better expose the dependence on r and the parameters held constant; the $Ra_h|_{(11)}$ symbol in the denominator under the square root is a shorthand for the rhs of the marginal stability relation (11). The fastest growing mode is the easiest to estimate graphically; otherwise a 6th-order polynomial needs to be evaluated, see also [76]. The thicker $p_1(k^2)$ curve in Fig. 19, corresponding to the case at hand, has the maximum at $k_f = 1.33\ \mathrm{km}^{-1}$, or the wavelength $\lambda_f = 5.5$ km, consistent with the solution patterns in Fig. 17 and the first pair of the extrema in Fig. 18. The mode (12) critical at $Ra_h \approx 2$, at $Ra_h \approx 77$ grows roughly three times slower than the fastest growing mode λ_f.

To further document the utility of the linear theory for analysis of under-resolved simulations of convective fields, we supplement the experiments highlighted in Fig. 17 with calculations employing explicit constant viscosities ν_h and ν_v, such that $\nu_v = 2.5\ \mathrm{m}^2\ \mathrm{s}^{-1}$ but ν_h changes accordingly to produce a range of anisotropy ratios centered at $r = 1/170$. Fig. 20 highlights the resulting w fields with the $r = 2^l/170;\ l = -1, 1$ results; whereas Fig. 21 summarizes the full range of calculations against the linear theory predictions. The full circles delineate the fastest growing modes at the maxima of $p_1(k^2)$ curves, including these in Fig. 19; whereas full squares delineate the relation (14) for the critical modes (12). The empty circles mark

the dominant simulated modes determined from the analysis of the corresponding structure and autocorrelation functions against w fields. The key outcome is an approximate inverse proportionality of the band of unstable modes' wavelengths to $\sqrt{r}$. This extends the earlier arguments in [41,43,44] beyond the marginal stability relations and the canonical scaling in (14). As r increases, v_h decreases and the effective Ra_h grows, so there is a tendency (Fig. 21) for the band of the dominant modes to shrink toward the range of wavelengths observed in the LES or ILES results (Figs. 7 or 13) free of enhanced filters. This dependency of scale selection on r corroborates the prevailing impact of filtering and associated moderate Rayleigh number effects on the organization of convection in under-resolved simulations.

6. Concluding remarks

The main stream of research in geophysical and astrophysical convection falls in the regime of large Rayleigh numbers. Rapid progress in computational technology already enables large- and global-scale simulations of convective fields at unprecedented mesoscale resolutions. This enables calculations free of convection parameterizations (viz. phenomenological models), in the spirit of LES. Ironically, the simulated (as opposed to parameterized) convection can be largely under-resolved, making numerical solutions sensitive to ad hoc filtering present in some form in all computational models. The latter shifts the virtual reality of convection toward moderate and low Rayleigh number regimes, rich in intriguing and attractive forms of the structural organization, yet unrealistic for the specified external parameter range.

Numerical artifacts such as implicit numerical viscosity and dispersion are widely covered in text-books on numerical methods, yet there appears to be a need for appreciating "implicit numerical topology" while analyzing under-resolved convective structures. Ultimately, the ambition is to develop skills and tools for identifying and improving upon such spurious effects. It turns out that the classical theoretical apparatus for low and moderate Rayleigh number convection, can be adapted to the virtual reality of under-resolved large-eddy-simulation to provide effective means for separating spurious effects from the coarse-grained truth of well resolved large eddies.

To document the impact of effective model viscosity on the structure of convective fields, we performed a large series of simulations mimicking a typical scenario in atmospheric models with resolution hypothetically adequate in the vertical but too coarse in the horizontal. Effectively, this amounts to admitting large anisotropy of viscous effects. In this context, we performed an extensive structural convergence analysis and documented differences between "realistic" cellular convection and the spurious structures. Comparing various means of enhancing the effective viscosity in the horizontal at a constant anisotropy ratio, we found that the details of filtering are inessential, and that the common denominator of the scale selection is consistent with the classical linear theory adapted here to a small anisotropy ratio at moderate Rayleigh numbers.

On the practical side, this study documents that some numerical approaches to convection simulation may be preferable when the resolution is inadequate. While control of effective numerical viscosity is certainly the key to quality results, resorting to non-dissipative numerics is not a cure.[7] Implicit LES appears to better represent coarsened, well resolved simulations than standard explicit LES. However, not every dissipative approach has adequate implicit LES properties. For instance, any numerical viscosity that depends on the magnitude of the flow, as opposed to its derivatives, is potentially prone to evincing spurious effects. Non-oscillatory forward-in-time (NFT) methods based on MPDATA advection appear well suited for under-resolved simulations as they are numerically isotropic and their nonlinear stability does not depend on explicit filters or subgrid-scale models.

Acknowledgments

Personal reviews by Robert Sharman and Nils Wedi and comments from two anonymous referees are gratefully acknowledged. This work was supported in part by the DOE Award # DE-FG02-08ER64535 and the Polish Ministry of Science and Higher Education. Computer time was provided by NSF MRI Grant CNS-0421498, NSF MRI Grant CNS-0420873, NSF MRI Grant CNS-0420985, NSF sponsorship of the National Center for Atmospheric Research, the University of Colorado, and a grant from the IBM Shared University Research (SUR) program. The National Center for Atmospheric Research is sponsored by the National Science Foundation.

References

[1] F.J. Robinson, K.L. Chan, Non-Boussinesq simulations of Rayleigh–Bénard convection in a perfect gas, Phys. Fluids 16 (2004) 1321–1333.
[2] W.W. Grabowski, MJO-like coherent structures: sensitivity simulations using the cloud-resolving convection parameterization (CRCP), J. Atmos. Sci. 60 (2003) 847–864.
[3] F.J. Robinson, K.L. Chan, A large-eddy simulation of turbulent compressible convection: differential rotation in the solar convection zone, Mon. Not. Roy. Astron. Soc. 321 (2001) 723–732.
[4] E. Bodenschatz, W. Pesch, G. Ahlers, Recent developments in Rayleigh–Bénard convection, Annu. Rev. Fluid Mech. 32 (2000) 709–778.
[5] K.A. Emanuel, D.J. Raymond, The Representation of Cumulus Convection in Numerical Models, American Meteorological Society, 1993.
[6] P.K. Smolarkiewicz, T.L. Clark, Numerical simulation of the evolution of a three-dimensional field of cumulus clouds. Part I: Model description, comparison with observations and sensitivity studies, J. Atmos. Sci. 42 (1985) 502–521.
[7] J.W.M. Cuijpers, P.G. Duynkerke, Large eddy simulation of trade wind cumulus clouds, J. Atmos. Sci. 50 (1993) 3894–3908.

[7] Noteworthy, reducing the anisotropy of model filters by enhancing viscosity in the "vertical" can improve the prediction of convection organization [77].

[8] W.W. Grabowski, P. Bechtold, A. Cheng, R. Forbes, C. Halliwell, M. Khairoutdinov, S. Lang, T. Nasuno, J. Petch, W.K. Tao, et al, Daytime convective development over land: a model intercomparison based on LBA observations, Q. J. Roy. Meteorol. Soc. 132 (2006) 317–344.
[9] W.C. Skamarock, J.B. Klemp, A time-split nonhydrostatic atmospheric model for weather research and forecasting applications, J. Comput. Phys. 227 (2008) 3465–3485.
[10] M. Satoh, T. Matsuno, H. Tomita, H. Miura, T. Nasuno, S. Iga, Nonhydrostatic icosahedral atmospheric model (NICAM) for global cloud resolving simulations, J. Comput. Phys. 227 (2008) 3486–3514.
[11] J. Done, C.A. Davis, M. Weisman, The next generation of NWP: explicit forecasts of convection using the weather research and forecasting (WRF) model, Atmos. Sci. Lett. 5 (2004) 110–117.
[12] W.C. Skamarock, Evaluating mesoscale NWP models using kinetic energy spectra, Mon. Weather Rev. 132 (2004) 3019–3032.
[13] D.E. Stevens, A.S. Ackerman, C.S. Bretherton, Effects of domain size and numerical resolution on the simulation of shallow cumulus convection, J. Atmos. Sci. 59 (2002) 3285–3301.
[14] G.H. Bryan, J.C. Wyngaard, J.M. Fritsch, Resolution requirements for the simulation of deep moist convection, Mon. Weather Rev. 131 (2003) 2394–2416.
[15] M. Wheeler, G.N. Kiladis, Convectively coupled equatorial waves: analysis of clouds and temperature in the wave number-frequency domain, J. Atmos. Sci. 56 (1999) 374–399.
[16] B. Brümmer, Roll and cell convection in wintertime Arctic cold-air outbreaks, J. Atmos. Sci. 56 (1999) 2613–2636.
[17] O. Fuhrer, C. Schär, Embedded cellular convection in moist flow past topography, J. Atmos. Sci. 62 (2005) 2810–2828.
[18] D.J. Kirshbaum, D.R. Durran, Atmospheric factors governing banded orographic convection, J. Atmos. Sci. 62 (2005) 3758–3774.
[19] A.V. Getling, Rayleigh–Bénard Convection Structures and Dynamics, World Scientific, 1998.
[20] S. Bernard-Trottolo, B. Campistron, A. Druilhet, F. Lohou, F. Saïd, TRAC98: detection of coherent structures in convective boundary layer using airborne measurements, Bound.-Lay. Meteorol. 111 (2004) 181–224.
[21] B.D. Pollard, S. Khanna, S.J. Frasier, J.C. Wyngaard, D.W. Thomson, R.E. McIntosh, Local structure of the convective boundary layer from a volume-imaging radar, J. Atmos. Sci. 57 (2000) 2281–2296.
[22] H. Schmidt, U. Schumann, Coherent structure of the convective boundary layer derived from large-eddy simulations, J. Fluid Mech. 200 (1989) 511–562.
[23] B.W. Atkinson, J.W. Zhang, Mesoscale shallow convection in the atmosphere, Rev. Geophys. 34 (1996) 403–431.
[24] J. Krawczyk, Z. Piotrowski, B. Jakubiak, S.P. Malinowski, L. Lobocki, High resolution modelling of atmospheric flow over southern Poland, in: Abstracts Book and CD-ROM Proceedings, 21st International Congress of Theoretical and Applied Mechanics, August 15–21, Warsaw, Poland.
[25] M. Niezgodka, B. Jakubiak, Scientific aspects of numerical weather prediction at ICM, in: Research Works Based on the ICMs UMPL Numerical Weather Prediction System Results, Wydawnictwa ICM, 2002, ISBN 83-917150-0-0.
[26] J.M. Prusa, P.K. Smolarkiewicz, A.A. Wyszogrodzki, EULAG, a computational model for multiscale flows, Comput. Fluids 37 (2008) 1193–1207.
[27] J. Clyne, P. Mininni, A. Norton, M. Rast, Interactive desktop analysis of high resolution simulations: application to turbulent plume dynamics and current sheet formation, New J. Phys. 9 (2007) 301.
[28] P.K. Smolarkiewicz, L.G. Margolin, MPDATA: a finite-difference solver for geophysical flows, J. Comput. Phys. 140 (1998) 459–480.
[29] P.K. Smolarkiewicz, Multidimensional positive definite advection transport algorithm: an overview, Int. J. Numer. Methods Fluids 50 (2006) 1123–1144.
[30] R. Liska, B. Wendroff, Composite schemes for conservation laws, SIAM J. Numer. Anal. 35 (1998) 2250–2271.
[31] R. Liska, B. Wendroff, Two-dimensional shallow water equations by composite schemes, Int. J Numer. Methods Fluids 30 (1999) 461–479.
[32] W.W. Grabowski, P.K. Smolarkiewicz, Monotone finite-difference approximations to the advection–condensation problem, Mon. Weather Rev. 118 (1990) 2082–2097.
[33] R.H. Miller, A horror story about integration methods, J. Comput. Phys. 93 (1991) 469–476.
[34] D. Drikakis, L.G. Margolin, P.K. Smolarkiewicz, On spurious eddies, Int. J. Numer. Methods Fluids 40 (2002) 313–322.
[35] L. Rayleigh, On convection currents in a horizontal layer of fluid, when the higher temperature is on the under side, Philos. Mag. 32 (1916) 529–546.
[36] H. Bénard, Les tourbillons cellulaires dans une nappe liquide, Rev. Gen. Sci. Pures Appl. 11 (1900) 1261–1271.
[37] S. Chandrasekhar, Hydrodynamic and Hydromagnetic Stability, Courier Dover Publications, 1981.
[38] L.D. Landau, E.M. Lifshitz, Course of Theoretical Physics, Fluid Mechanics, vol. 6, Pergamon Press, 1987.
[39] P. Drazin, W. Reid, Hydrodynamic Stability, Cambridge University Press, 2004.
[40] H. Jeffreys, Some cases of instability in fluid motion, Proc. Roy. Soc. Lond. A 118 (1928) 195–208.
[41] C.H.B. Priestley, The width-height ratio of large convection cells, Tellus 14 (1962) 123–124.
[42] A. Krueger, S. Fritz, Cellular cloud patterns revealed by TIROS I, Tellus 13 (1961) 1–7.
[43] D. Ray, Cellular convection with nonisotropic eddys, Tellus 17 (1965) 434–439.
[44] P.J. Sheu, E.M. Agee, J.J. Tribbia, A numerical study of physical processes affecting convective cellular geometry, J. Meteorol. Soc. Jpn. 58 (1980) 489–499.
[45] G.P. Williams, Friction term formulation and convective instability in a shallow atmosphere, J. Atmos. Sci. 29 (1972) 870–876.
[46] D. Ray, Variable eddy diffusivities and atmospheric cellular convection, Bound.-Lay. Meteorol. 36 (1986) 117–131.
[47] R.D. Smith, J.C. McWilliams, Anisotropic horizontal viscosity for ocean models, Ocean Modell. 5 (2003) 129–156.
[48] Z.P. Piotrowski, Numerical simulation of thermal convection, Ph.D. Thesis, University of Warsaw (in preparation).
[49] P.K. Smolarkiewicz, L.G. Margolin, A.A. Wyszogrodzki, A class of nonhydrostatic global models, J. Atmos. Sci. 58 (2001) 349–364.
[50] N.P. Wedi, P.K. Smolarkiewicz, Extending Gal-Chen and Somerville terrain-following coordinate transformation on time-dependent curvilinear boundaries, J. Atmos. Sci. 193 (2004) 1–20.
[51] P.K. Smolarkiewicz, J. Szmelter, Iterated upwind schemes for gas dynamics, J. Comput. Phys. 228 (2009) 33–54.
[52] J.M. Prusa, P.K. Smolarkiewicz, An all-scale anelastic model for geophysical flows: dynamic grid deformation, J. Comput. Phys. 190 (2003) 601–622.
[53] P.K. Smolarkiewicz, J.M. Prusa, Towards mesh adaptivity for geophysical turbulence: continuous mapping approach, Int. J. Numer. Methods Fluids 47 (2005) 789–801.
[54] F.B. Lipps, R.S. Hemmler, A scale analysis of deep moist convection and some related numerical calculations, J. Atmos. Sci. 39 (1982) 2192–2210.
[55] T.L. Clark, R.D. Farley, Severe downslope windstorm calculations in two and three spatial dimensions using anelastic interactive grid nesting: a possible mechanism for gustiness, J. Atmos. Sci. 41 (1984) 329–350.
[56] U. Schumann, Subgrid length-scales for large-eddy simulation of stratified turbulence, Theor. Comput. Fluid Dyn. 2 (1991) 279–290.
[57] L.G. Margolin, P.K. Smolarkiewicz, Z. Sorbjan, Large-eddy simulations of convective boundary layers using nonoscillatory differencing, Physica D 133 (1999) 390–397.
[58] P.K. Smolarkiewicz, J.M. Prusa, Forward-in-time differencing for fluids: simulations of geophysical turbulence, in: D. Drikakis, B.J. Guertz (Eds.), Turbulent Flow Computation, Kluwer Academic Publishers, 2002, pp. 279–312.
[59] P.K. Smolarkiewicz, R. Sharman, J. Weil, S.G. Perry, D. Heist, G. Bowker, Building resolving large-eddy simulations and comparison with wind tunnel experiments, J. Comput. Phys. 227 (2007) 633–653.
[60] C.S. Cotter, P.K. Smolarkiewicz, I.N. Szczyrba, A viscoelastic model for brain injuries, Int. J. Numer. Methods Fluids 40 (2002) 303–311.
[61] A. Warn-Varnas, J. Hawkins, P.K. Smolarkiewicz, S.A. Chin-Bing, D. King, Z. Hallock, Solitary wave effects north of Strait of Messina, Ocean Modell. 18 (2007) 97–121.
[62] N.P. Wedi, P.K. Smolarkiewicz, Direct numerical simulation of the Plumb–McEwan laboratory analog of the QBO, J. Atmos. Sci. 63 (2006) 3226–3252.
[63] M.L. Waite, P.K. Smolarkiewicz, Instability and breakdown of a vertical vortex pair in a strongly stratified fluid, J. Fluid Mech. 606 (2008) 239–273.

[64] W.J. Rider, The relationship of MPDATA to other high-resolution methods, Int. J. Numer. Methods Fluids 50 (2006) 1145–1158.
[65] L.G. Margolin, P.K. Smolarkiewicz, A.A. Wyszogrodzki, Implicit turbulence modeling for high Reynolds number flows, J. Fluids Eng. – Trans. ASME 124 (2002) 862–867.
[66] J.A. Domaradzki, Z. Xiao, P.K. Smolarkiewicz, Effective eddy viscosities in implicit large eddy simulations of turbulent flows, Phys. Fluids 15 (2003) 3890–3893.
[67] L.G. Margolin, W.J. Rider, F.F. Grinstein, Modeling turbulent flow with implicit LES, J. Turbul. 7 (2006) 1–27.
[68] L.G. Margolin, P.K. Smolarkiewicz, A.A. Wyszogrodzki, Dissipation in implicit turbulence models: a computational study, J. Appl. Mech. – Trans. ASME 73 (2006) 469–473.
[69] P.K. Smolarkiewicz, L.G. Margolin, Studies in geophysics, in: F.F. Grinstein, L.G. Margolin, W. Rider (Eds.), Implicit Large Eddy Simulation: Computing Turbulent Fluid Dynamics, Cambridge University Press, 2007, pp. 423–438.
[70] B.W. Shen, R. Atlas, J.D. Chern, O. Reale, S.J. Lin, T. Lee, J. Chang, The 0.125 degree finite-volume general circulation model on the NASA Columbia supercomputer: preliminary simulations of mesoscale vortices, Geophys. Res. Lett. 33 (2006) L05801.
[71] G.S. Young, D.A.R. Kristovich, M.R. Hjelmfelt, R.C. Foster, Rolls, streets, waves, and more: a review of quasi-two-dimensional structures in the atmospheric boundary layer, Bull. Am. Meteorol. Soc. 83 (2002) 997–1001.
[72] B.D. Ripley, Pattern Recognition and Neural Networks, Cambridge University Press, 1996.
[73] M. Cullen, D. Salmond, P.K. Smolarkiewicz, Key numerical issues for future development of the ECMWF model, in: Proceedings of the ECMWF Workshop on Developments in Numerical Methods for Very High Resolution Global Models, Reading, UK, ECMWF, 5–7 June 2000, pp. 183–206.
[74] S. Hickel, N.A. Adams, J.A. Domaradzki, An adaptive local deconvolution method for implicit LES, J. Comput. Phys. 213 (2006) 413–436.
[75] T.L. Clark, T. Hauf, J.P. Kuettner, Convectively forced internal gravity-waves: results from two-dimensional numerical experiments, Q. J. Roy. Meteorol. Soc. 112 (1986) 899–925.
[76] S. Fauve, Pattern forming instabilities, in: C. Godrèche, P. Manneville (Eds.), Hydrodynamics and Nonlinear Instabilities, Cambridge University Press, 1998, pp. 387–491.
[77] F. Váňa, P. Bénard, J.F. Geleyn, A. Simon, Y. Seity, Semi-Lagrangian advection scheme with controlled damping: an alternative to nonlinear horizontal diffusion in a numerical weather prediction model, Q. J. Roy. Meteorol. Soc. 134 (2008) 523–537.